

3D reconstruction from radiologic projections applied
to dental implantology and to oral-facial surgery

Reconstruction 3D à partir de projections
radiologiques appliquée au cadre de l'implantologie
dentaire et de la chirurgie oro-faciale

Antonio Moreno, Isabelle Bloch, Julien Dutreuil and Manuel Deval

École Nationale Supérieure des Télécommunications

Département TSI - CNRS UMR 5141 LTCI

46 rue Barrault, 75634 Paris Cedex 13, France

Tel: +33 1 45 81 72 04

Fax: +33 1 45 81 37 94

E-mail: moreno@tsi.enst.fr

Contents

1	Introduction	8
2	State of the art in reconstruction and choice of the reconstruction method	12
2.1	Physical principle	12
2.2	Reconstruction principle	12
2.2.1	General introduction to 2D and 3D tomographic imagery	12
2.2.2	2D computer assisted tomography	14
2.2.3	3D computer assisted tomography	16
2.3	Choice and description of criteria for comparing reconstruction methods . .	17
2.4	3D reconstruction methods	19
2.4.1	Problem nature	19
2.4.2	Analytical methods	20
2.4.3	Algebraic methods	24
2.4.4	Statistical methods	31
2.4.5	Structural methods	36
2.4.6	Other methods	38
2.5	Choice of the method	38
3	Regularized reconstruction	40
3.1	Regularization principle	40
3.2	Choice of the regularization term	42
3.2.1	Adaptation to ART methods	42
3.2.2	The potential function	42
3.2.3	The positivity term	43
3.2.4	The energy function to minimize	44
3.3	Optimization method	44
4	3D regularized reconstruction from a small number of projections in maxillo-facial imaging: feasibility and first experimental results	48
4.1	Simulator	48
4.1.1	Available data	48
4.1.2	The objective of the simulator	49
4.1.3	System geometry	49
4.1.4	Interface	51
4.1.5	Geometrical construction	52

4.1.6	Projection implementation	54
4.1.7	Filtering	55
4.2	Reconstruction implementation	56
4.2.1	The projection matrix	56
4.2.2	The reconstruction volume	59
4.3	Tests and measures	59
4.3.1	Influence of the number of projections	60
4.3.2	Influence of the regularization functions	61
4.3.3	The optimal parameters of the regularization function	63
4.4	Conclusion	64
5	Conclusion and future work	70
A	Introduction to the Radon transform	72
A.1	Definition	72
A.2	Inversion formulas [29]	72
B	Projection theorem	74
C	3D backprojection operator	75
D	Bayesian estimation	77
E	Maximum of Entropy Principle	79
F	Minimization algorithm of Delaney and Bresler [8]	80
G	Implementation of the semi-quadratic minimization algorithm	81
H	The reconstruction implementation	83
I	Strange effects of wrong regularization	86

List of Figures

1.1	Planning interface. The different sagittal cuts of the jaw and the dental canal can be observed.	10
1.2	Virtual reality view superimposed over real view during an operation. . . .	10
1.3	Scheme of the main parts of a sagittal cut of the jaw (right) compared with a real sagittal cut (left).	11
2.1	Principle of a real 3D acquisition from a conical source of X rays.	14
2.2	A projection definition in 2D parallel geometry.	15
2.3	Discretization of f : a) in 2D, b) in 3D.	26
3.1	The parameter α in the Huber function	44
4.1	Absolute coordinate system.	50
4.2	An example of the absolute coordinate system from different points of view. From top to bottom and from left to right: view from the left side, view from the right side, front view, upper view, bottom view.	50
4.3	Parallelepiped defined by the sensor and the emitter: P_0, P_1, P_2, P_3 (the sensor corners) and C (the sensor center) define the sensor or projection plane; Q_0, Q_1, Q_2, Q_3 (the emitter corners) and C' (the emitter center) define the emitter plane.	51
4.4	Relative coordinate system diagram.	52
4.5	The simulator interface.	53
4.6	Some examples of projected images. On the left, two simulated radiographies with a pixel size of 0.5 mm. On the right side, the resolution is 1 mm/pixel.	55
4.7	Geometrical explanation to find the ϵ_{ideal} for filtering. The cube represents a voxel.	56
4.8	Projection matrix structure.	57
4.9	Matrix ray.	58
4.10	RMSE comparison for reconstruction with a different number of projections.	60
4.11	RMSE comparison for several λ and α (from Huber's function) combinations when 4 projections (left) and 8 projections (right) are used for the reconstruction.	61
4.12	RMSE comparison for different regularization functions on the phantom image. Number of iterations = 100; Number of projections = 4.	65
4.13	RMSE comparison for different regularization functions on the phantom image. Number of iterations = 100; Number of projections = 8.	65

4.14	RMSE comparison for different combinations of λ and α with 4 projections on a phantom image. The potential function used is Huber's one and the number of iterations is 100.	67
4.15	RMSE comparison for different combinations of λ and α with 8 projections on a phantom image. The potential function used is Huber's one and the number of iterations is 100.	67
4.16	RMSE comparison for different combinations of λ and α with 4 projections on a dry jaw. The potential function used is Huber's one and the number of iterations is 100.	68
4.17	RMSE comparison for different combinations of λ and α with 8 projections on a dry jaw. The potential function used is Huber's one and the number of iterations is 100.	68
4.18	RMSE comparison for different combinations of λ and α with 4 projections for an <i>in vivo</i> application. The potential function used is Huber's one and the number of iterations is 100.	69
4.19	RMSE comparison for different combinations of λ and α with 8 projections for an <i>in vivo</i> application. The potential function used is Huber's one and the number of iterations is 100.	69
C.1	Projection of a vector r on a plane π_τ	76

List of Tables

2.1	List of criteria for the choice of a reconstruction method. Priorities are quantified from 0 –necessary criteria– to 5 –unimportant criteria–.	19
3.1	Convex potential functions.	43
4.1	Comparative table of a resulting reconstructed cut of the phantom for 1000 iterations.	62
4.2	Comparative table of resulting reconstructed cuts of the jaw for 100 iterations.	66
I.1	Some strange effects of regularization that we have obtained with an inappropriate choice of the parameters for a cut of the phantom.	86

Abstract

We try to develop a light medical three-dimensional imaging system to use it in dental environment. This system must allow to locate the smallest anatomical structures with a very good precision in a small volume. It will avoid using heavy CT scanner exams.

As in CT (*Computed Tomography*), the researched medical image represents 3D distribution of the “bone densities” (X ray absorption) in the zone we want to study. Thanks to a technique close to tomography, this image can be obtained by reconstruction from a digital radiographies set (projection images of the structure).

Although the acquisition of every projection is short in time and produces little radiation, it is very important to control the number of views to have a system as light as possible, the least invasive for the patient and, so, as operational as possible. The patient’s mouth anatomy constraints a lot the angles to take the radiologic projections. The orientation of these projections will influence on the reconstruction quality as much as the number of views.

Therefore, the main criteria for this reconstruction are:

- the quality in terms of likelihood and precision of the reconstruction;
- the number, the precision and the orientations of the necessary views;
- the processing speed (depending on the number of views).

A compromise should be found taking account of these various criteria.

Keywords:

Inverse problem, reconstruction, 3D, radiology, algebraic methods, projections, dental surgery, implants, dental canal, pattern recognition.

Résumé

Nous cherchons à développer un système d'imagerie médicale tridimensionnel léger dédié à une utilisation en milieu dentaire. Ce système doit permettre de localiser des fines structures anatomiques avec une grande précision dans un petit volume d'étude. Il nous permettra de nous affranchir des lourdeurs de l'utilisation du scanner.

Comme dans le CT (*Computed Tomography*), l'image médicale recherchée représente la distribution tridimensionnelle des "densités des tissus" (absorption des rayons X) sur la zone d'étude. Grâce à une technique proche de la tomographie, cette image peut être obtenue par reconstruction à partir d'une série de radiographies numériques (images en projection de la structure recherchée).

Bien que l'acquisition de chacune des projections soit courte et peut être irradiante, il est primordial de contrôler le nombre de vues pour rendre le système le plus léger possible, le moins invasif pour le patient et, donc, plus opérationnel possible. L'anatomie de la bouche du patient contraint fortement les angles de prise de vue accessibles. Au même titre que le nombre de vues, l'orientation de ces vues influera donc sur la qualité de la reconstruction.

Les critères principaux pour cette reconstruction sont alors:

- la qualité en terme d'incertitude et de finesse de la reconstruction ;
- le nombre, la précision et les orientations de vues nécessaires ;
- la rapidité du traitement (en fonction du nombre de vues).

Il faut trouver un compromis tenant compte de ces différents critères.

Mot-clés :

Problème inverse, reconstruction, 3D, radiologie, méthodes algébriques, projections, chirurgie dentaire, implants, nerf dentaire, reconnaissance des formes.

Chapter 1

Introduction

3D reconstruction from radiographic projections is a widely addressed problem in the medical imaging literature. However, no application has been found so far in the mandibular reconstruction field. Dentist requirements are very specific and induce particular constraints:

- the information to be found is very specific: cortical bone and dental canal should be accurately reconstructed;
- 3D densities of the bone are important, which calls for a volumetric reconstruction, not only a surface one;
- the input data consist of very few radiographic projections (typically up to 8) and in very limited positions (due to anatomical constraints).

These constraints led us to develop an approach consisting of a reconstruction part and a regularization method (to constrain the reconstruction with some *a priori* information and to deal with the reduced number of projections).

The contribution of this report is to show that regularized algebraic reconstruction is well adapted to this problem and to provide an experimental study for parameter optimization. It extends our preliminary work presented in [24].

Medical context

The imagery systems used in medical applications are very different. For example:

- MRI (Magnetic Resonance Imaging) furnishes anatomical data with good precision,
- X-ray techniques (such as tomography and tomosynthesis) also provide anatomical information,
- echography is used for surface reconstruction,
- SPECT and PET furnish functional information.

In our case, we are working with an X-ray technique which is between tomography and tomosynthesis (see [29] and [2]) as we have several projections placed in the 3D space, not only in a plane, and with variable angles.

The objective in our particular dental application is to avoid using Computed Tomography (CT scanner) because it implies going to a hospital (heavy system) and the quantity of radiations received by the patient is important. However, the dental environment has several constraints: the anatomy of the mouth (few permitted positions, with unequally distributed angles), the number of views (up to 8), the quality needed in the reconstruction (near the millimeter), the computing time (it must be low).

We work with a *navigation system* that is used to do dental surgery to put implants in the patient's jaw. First the dentist plans the operation with the interface shown in Figure 1.1 and then the intervention can be performed (Figure 1.2) using the navigation system.

We assume that this navigation system provides the exact sensor and emitter positions and their orientations and, therefore, we can have a *light* system for 3D reconstruction. The system provides the projections representing the attenuation of the matters crossed by the X rays from the source. This system is less heavy and less expensive than the "traditional" systems (scanner CT) and patients receive less radiation.

Objective

The objective is to perform a precise 3D reconstruction of a small part of the jaw. The main interest is to find the cortical bone and the dental canal. So, we are looking for a structure which looks in a sagittal cut schematically as in Figure 1.3.

Main stages

To reach this objective we have followed three main steps:

1. First, a bibliographic search has been done to find the most appropriate reconstruction method, based on a comparative study with respect to criteria adapted to our problem. We show that algebraic methods, such as ART, are the most suitable for our case. This is detailed in Chapter 2.
2. Once the reconstruction method has been chosen, we address the problem of regularization with the aim to obtain better results. This stage was inspired by [2] and [34] and is described in Chapter 3.
3. Finally we apply our regularized reconstruction method to simulated and real data and study the first experimental results and parameter optimization. Preliminary results on this have been published in [24] and a detailed description is given in Chapter 4.

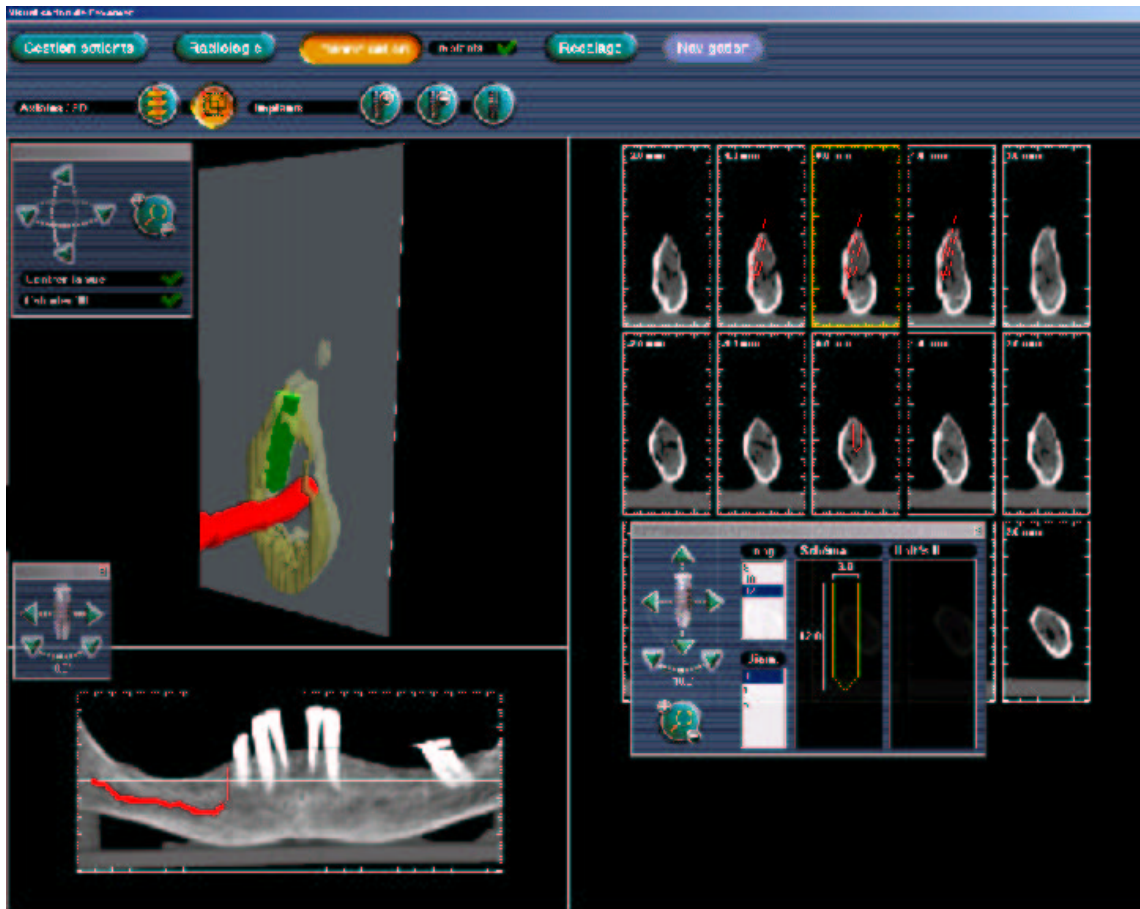


Figure 1.1: Planning interface. The different sagittal cuts of the jaw and the dental canal can be observed.

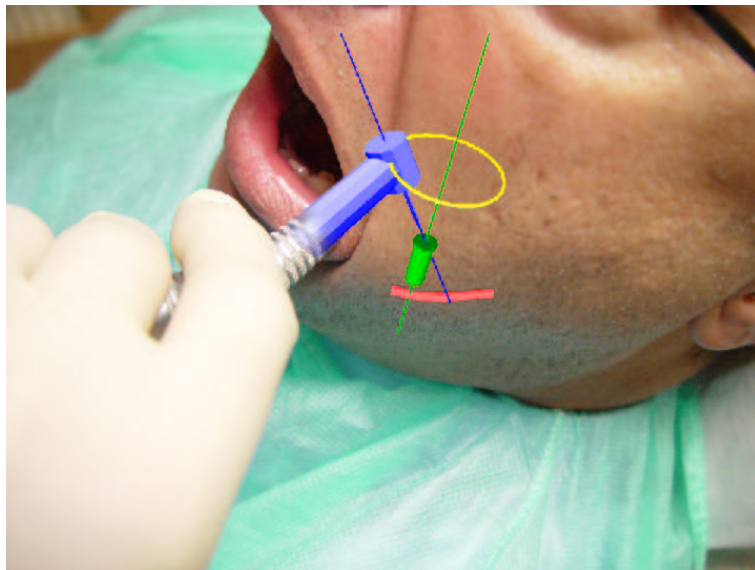


Figure 1.2: Virtual reality view superimposed over real view during an operation.

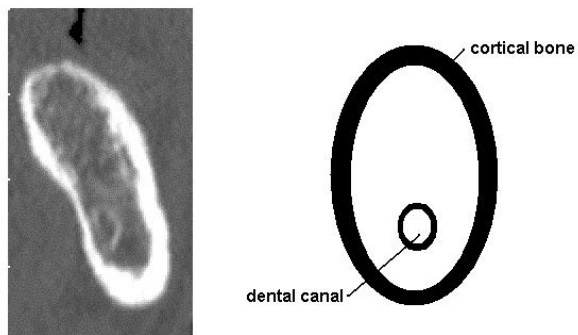


Figure 1.3: Scheme of the main parts of a sagittal cut of the jaw (right) compared with a real sagittal cut (left).

Chapter 2

State of the art in reconstruction and choice of the reconstruction method

3D reconstruction from radiographic projections is a largely studied subject in medical imaging. But, as mentioned previously, no application has been found in the dental field, where constraints are very specific.

In this chapter, we present the existing reconstruction methods and we discuss them in light of criteria adapted to our problem.

2.1 Physical principle

The physical principle used in X-ray tomography is the X-ray transmission through the matter. For the energy range used in medicine, the interaction between X photons and the matter can be observed by three phenomena: the photo-electric effect, the Compton diffusion effect and the Rayleigh diffusion effect, which are translated globally by an attenuation.

The modeling of the transmission by an integral on a right line relies, in a first approach, on the hypothesis of having a monochromatic X-ray beam.

The image $f(x, y)$ reconstructed in X-ray tomography corresponds to the distribution of the linear attenuation coefficient of the crossed matters in the considered cut.

More information about the physical principle can be found in [29], [2], [17], [28].

2.2 Reconstruction principle

2.2.1 General introduction to 2D and 3D tomographic imagery

For any physical radiation, the computer assisted tomography systems have the following principle in common:

- Indirect information is obtained from different incidences (projections) over a selected cut of the object.
- Next, this cut is expressed as a solution of an inverse problem and it is numerically reconstructed.

Even if the tomographic imagery has been a real progress in medicine, it is often insufficient to lead to a diagnosis. For instance, one tomographic cut only does not allow to have a good knowledge about the localization of a tumor (size, position,...), that is to say, it does not give a real three-dimensional information. For this reason, sometimes, we call this kind of reconstruction *half-3D* reconstruction. Tomography only gives an incomplete view (bidimensional) which can be difficult to place in the three-dimensional space. From now on, we will call “three-dimensional” image or 3D image the distribution of a physical parameter at every point of a three-dimensional space, which is the representation of a volume.

Usual tomographic systems allow to obtain 3D images by stacking a series of parallel cuts at different levels (sequential 3D). This technique is long, heavy and the representation of the obtained volume can be erroneous due to movement between cuts, to the non-simultaneity of different cuts if the examined organ is moving (the heart, for example) and to the different resolutions in the three directions of the space (usually the resolution is more precise in the cut plane than in the inter-cut direction). Obtaining an image of all the volume from one only acquisition will avoid all these disadvantages. This is called *real three-dimensional tomography*.

Real three-dimensional tomography includes techniques that allow to obtain, by an appropriate acquisition system, the image of a volume at a given instant. So, the computer assisted tomography principle for reconstruction of cuts (*half-3D reconstruction*) has to be generalized to define the computer assisted voludensitometry for volume reconstruction.

As an example, X tomography systems that allow a real 3D acquisition use usually a conical source of X rays which is moved around the object. For every source position, a radiography is obtained, which corresponds to a 2D projection of the 3D image to be reconstructed (see Figure 2.1). By moving the sensor-emitter system, a set of radiographies associated to a set of projections under different view angles is obtained, from which reconstruction has to be done.

A simplification has been chosen for an initial approach: a parallel source of X rays instead of a conical one is assumed in the following.

3D extensions have also been proposed for other modalities of tomographic imagery (for example in PET) and, in some way, the formalism developed in X tomography can be used.

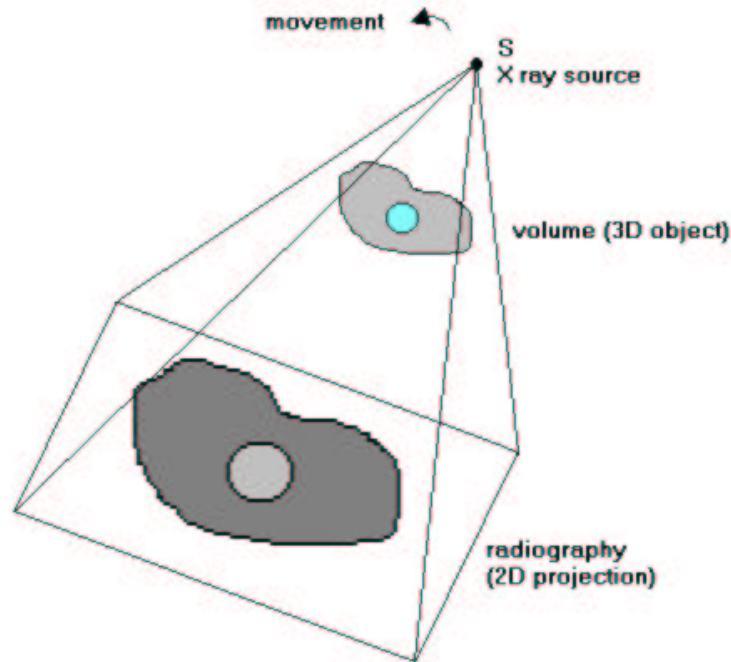


Figure 2.1: Principle of a real 3D acquisition from a conical source of X rays.

The problems in 3D reconstruction from 2D projections are of several natures:

- on the one hand, the theoretical point of view: the choice of the source trajectory, the number of projections, the definition of an adapted inversion method and of a 3D reconstruction algorithm. In our specific case, we do not really have a fixed trajectory of the source and the number of projections is very limited (see Section 4.1.3 for details);
- on the other hand, the technological point of view: the realization of an acquisition device and the conception of a computing system powerful enough to support the reconstruction algorithms and the manipulation of an important quantity of data.

In the next sections, we introduce the problem of 3D image reconstruction which generalizes the problem of 2D reconstruction from 1D projections. The acquisition of tomographic projections in 2D and in 3D relies on the Radon transform. See [29].

2.2.2 2D computer assisted tomography

Direct problem

In 2D computer assisted tomography the acquisition allows to obtain a set of 1D projections. Let $f(x, y)$ be the function to be reconstructed. We assume that it has a bounded

support D and that it is continuous and infinitely differentiable (of class C^∞). The (parallel) projection at point u on a line of direction θ , noted $p_\theta(u)$, is equal to the integral of f along a line of angle $\theta + \frac{\pi}{2}$:

$$p_\theta(u) = \int_{\mathbb{R}^2} f(x, y) \delta(x \cos \theta + y \sin \theta - u) dx dy \quad (2.1)$$

or as a simple integral:

$$p_\theta(u) = \int_{-\infty}^{+\infty} f(u \cos \theta - v \sin \theta, u \sin \theta + v \cos \theta) dv \quad (2.2)$$

The dotted line on Figure 2.2, specified by θ and u , on which the integration is done, is called *projection ray*.

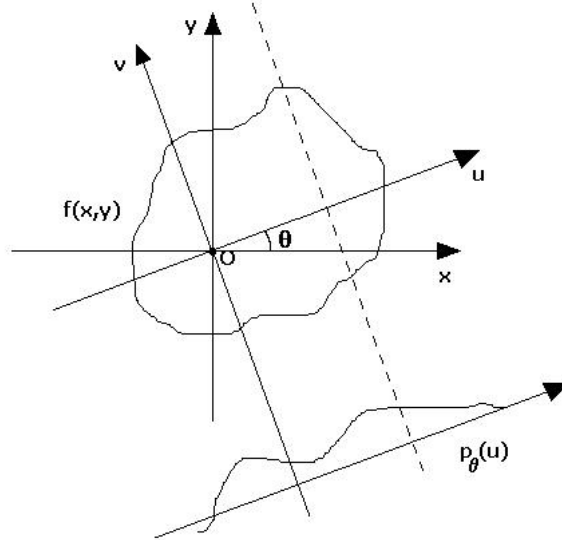


Figure 2.2: A projection definition in 2D parallel geometry.

The acquisition provides $\{p_\theta(u) / \theta \in [0, \pi[\text{ and } u \in \mathbb{R}\}^1$, that represents exactly the Radon transform of the image $f(x, y)$:

$$R f(u, \theta) = p_\theta(u) \quad (2.3)$$

So, the problem of 2D reconstruction is exactly equivalent to the problem of the Radon transform inversion (see Appendix A.1). Anyway, in practice, we use inversion formulas which are mathematically equivalent, but which are also more efficient from an algorithmic point of view.

¹The condition $\theta \in [0, \pi[$ assumes a symmetry of the attenuation: $p_\theta(u) = p_{\theta+\pi}(-u)$

Filtered backprojection algorithm

Using the projection theorem (Appendix B), and introducing the backprojection operator (described in Appendix A.2), the most widely used reconstruction formula is obtained.

In the 2D case, the backprojection operator consists in associating to the set of projections, an image, defined as:

$$Bp(x, y) = \int_0^\pi p_\theta(x \cos \theta + y \sin \theta) d\theta \quad (2.4)$$

This means that the reconstructed image will have at each point an intensity that is the sum of the values of the projections passing by this point. It can be shown that the backprojection of all the projections does not provide the original image, but a convoluted version of it. However, if the projections are appropriately filtered before backprojection, we can obtain the image. This is the classic principle of the “filtered backprojection algorithm”.

Discretization problems

In practice, data are sampled with regard to the number of projections and to the number of points in each projection. In addition to this, the reconstructed image in tomography is digital, represented by its coordinates on a specific basis. The continuous inversion formulas and the operators presented here above need some adaptations to be applied to the discrete case. So, a discrete backprojection operator must be defined, which will use an approximation of the integral and some interpolation models (see references in [29]).

The projection theorem and the Shannon theorem show that the sampling step of the projections determines the limit resolution accessible in the image. If the image contains some details lower than this limit, they are not correctly reconstructed because of the overlapping spectra phenomenon. In addition to this, the number of projections M that must be chosen can be connected, in an empiric way, to the number N of points by projection, by the relation $M = \pi N/2$. Generally, we admit that these conditions correspond to the reconstruction of an image of size $N \times N$. When the number of projections is too low, we obtain classically some artifacts (dark lines) on the reconstructed image. This was noticed in our first results (see Section 4.1.7 for more details).

More information on this aspects can be found in [3] and [29].

2.2.3 3D computer assisted tomography

The problem of 3D reconstruction consists in determining a function of three variables $f(x, y, z)$ from its bidimensional projections. The principle is the same than for the 2D case, but there are some important differences that must be taken into account. They are described in the following paragraphs.

Definition of projections

Divergent projections for a source position S are equal to the values of the function integrals on the right lines of the space going out the same point S . In X-ray tomography, this kind of projection corresponds to an acquisition using a conical source.

Parallel projections are equal to the values of the function integrals on right lines of the space parallel to each other. This type of projection can be considered as a limit case of a divergent projection where the source goes to infinity, or, in a practical way, when the distance source-object is large enough compared to the dimensions of the object so we can neglect the divergence.

The case of parallel projection is the one we have used as a first approach for our tests (Chapter 4).

Trajectory definition

The image $f(x, y, z)$ will have to be determined from a set of projections obtained for different positions of the source S . An acquisition is then completely determined by the type of projection (divergent or parallel) and by the data about the movement of the source. The main difference with the 2D case is that in 3D this movement has one more degree of freedom. The movement can be done either on a curvilinear trajectory (ring, spiral...) or on a surface (sphere, segment of a sphere...).

However, for our case, the different positions of the source do not inevitably follow a geometrical logic (see Section 4.1.3 for more details).

Backprojection operator

As in 2D, the backprojection operator has an important role in the theory of 3D images reconstruction. The divergent 3D backprojection operator is described in Appendix C.

More details can be found in [29].

2.3 Choice and description of criteria for comparing reconstruction methods

In order to compare the existing methods, we have defined a list of criteria according to the properties our method should fulfill.

- Our field of application and the second constraint (3D reconstruction of bone densities) impose obviously two criteria:
 - the method must be *applicable to 3D reconstruction* and
 - it must provide a *volumetric reconstruction* (not only the surface).

- Next, there are some very important criteria that are specific to our case:
 - the chosen method must allow the *addition of some a priori information* (constraints, regularization...) because we know that with a very small number of radiographic projections it is not possible to obtain a precise enough reconstruction;
 - due to important anatomical constraints, the acquisition geometry can not be fixed once for all, so our method must be *adaptable to different acquisition geometries*;
 - as we are working with real acquisitions from real sensors, noise will be present; that is why the chosen method must be *stable* (this implies convergence for iterative methods) and
 - for the same reason it must be *robust against noise*.
- The next three criteria will not have so much importance in a first stage, however if they limit the implementation results, they could become a priority. These criteria are:
 - the *memory cost*,
 - the *computing time* and
 - the *convergence speed* (number of iterations for the iterative methods).
- There are two more general characteristics that can be taken into account, even if they are not as relevant as the previous criteria:
 - *The implementation costs*, that is to say, if the method is easy or difficult to implement and
 - the fact that *the method has been already developed*, because this shows that the method can be used and that it works.

Table 2.1 summarizes these criteria and their importance. We have used priorities from 0 to 5:

- Priority 0 means that the criteria are absolutely necessary, that is to say that the methods that do not fulfill these criteria are not useful for our case. These characteristics are: *Applicable to 3D reconstruction* and *Volumetric reconstruction*.
- Priority 1 is used for criteria which are specific and very important for our case: *Addition of a priori information*, *Adaptable to different geometries*, *Stable* and *Robust against noise*.
- Priority 2 identifies the criteria which can limit the use of the method due to the fact that the method is too slow (*Computing time* criterion) or it consumes too much memory (*Memory cost* criterion). These criteria could become more important and some methods could be discarded because of them.

- Priority 3 is used for the criterion *Convergence speed* (number of iterations) and means that it is less important than the previous ones, because it is “included” somehow in the *Computing time* criterion.
- Priority 4 is used for the criteria which add some information about the method but will not be really decisive (*Implementation cost* and *Already developed*).
- Priority 5 identifies the criteria that are not important. As there would be too many and they are not interesting for our case, they are not detailed in this table.

	Criteria	Priority
<i>a</i>	Applicable to 3D reconstruction	0
<i>b</i>	Volumetric reconstruction	0
<i>c</i>	Addition of <i>a priori</i> information	1
<i>d</i>	Adaptable to different geometries	1
<i>e</i>	Stable	1
<i>f</i>	Robust against noise	1
<i>g</i>	Implementation cost	4
<i>h</i>	Already developed	4
<i>i</i>	Memory cost	2
<i>j</i>	Computing time	2
<i>k</i>	Convergence speed	3

Table 2.1: List of criteria for the choice of a reconstruction method. Priorities are quantified from 0 –necessary criteria– to 5 –unimportant criteria–.

2.4 3D reconstruction methods

In this section, we briefly present the existing reconstruction methods and we discuss their adaptation for our case as well as their appropriateness according to the previously described criteria.

2.4.1 Problem nature

As shown by the expressions of projections, the reconstruction calls for an inverse problem.

Before trying to inverse the problem, it is natural to ask oneself if the reconstruction problem from projections is well-posed or ill-posed. According to the literature, the problems of conditioning are not too crucial in tomographic reconstruction from a complete set of data. However, when the angle of view is limited, the problem can become severely ill-posed. The nature of the problem is a function of the diminution towards zero of the singular values of the operator. From the spectra decomposition of the 2D Radon transform, and taking into account only a finite number of singular values, we can observe

that the singular values are almost divided in two groups: in the first one, each singular value is near to the value obtained for a complete set of data, and in the other group, they are near to zero. The second group, which is more important when the data are incomplete, translates the bad conditioning of the problem. Anyway, we can see that it will be possible to reconstruct the components of the image linked to the singular functions associated to the singular values of the first group.

In X-ray tomography, the constraints about acquisition time, for instance, in the industrial field (the dental application described in Chapter 1 for example), allow the acquisition of only several very noisy projections (< 8). It is the same thing if we want to reconstruct an object that is moving (for example, the heart, in the medical field). In these different particular cases, the 3D reconstruction methods must be adapted to correct or to take into account some approximations, and to include some regularization techniques to avoid the instabilities that come from a bad conditioning of the inverse problem and from data noise.

There is a lot of (and very redundant) literature relative to reconstruction of tomographic images, either 2D or 3D. Similar techniques have been proposed and implemented independently, by different authors, in different fields and for different applications. According to [29], where there is a very complete synthesis of most existent methods, the reconstruction techniques can be classified in four different classes:

- The *analytical methods*. These methods consider a continuous approach to the problem for which an analytical inversion formula is searched.
- The *algebraic methods*. They consider a discrete approach to the problem, which is treated as the inversion of a linear system.
- The *statistical methods*. These methods use a probabilistic modeling of the data and/or the solutions.
- The *structural methods*. They are based on a more descriptive model, approaching the techniques used in computer vision.

2.4.2 Analytical methods

Analytical methods are based on a continuous modeling of the direct problem, expressed by Equation 2.1 in the 2D case. The searched solution is a continuous function in a Hilbert space, on which we will eventually be led to do additional assumptions and it is expressed by an analytical inversion formula. The fact that the reconstructed image and the data are discrete is just taken into account for the approximation of the inversion formula.

Because of their principle, the analytical methods take into account the acquisition geometry (type of projection and source trajectory). Most of the inversion formulas have been developed, in a first step, in the 2D case or in 3D for parallel acquisition geometries.

More details about analytical methods can be found in [3], [4], [29], [36], [21], [13] or [28].

Here we present the existing analytical methods and their characteristics:

– **3D reconstruction algorithm from conical projections by 3D deconvolution**

The principle of this method consists in:

- calculating the corrected backprojection of all conical projections and
- doing the deconvolution of the result.

This method is very sensitive to the number of views (projections) and this could deteriorate the image resolution.

The advantages of this method are that it has not a very high sensibility to noise (f) as backprojection reduces additive Gaussian noise and that computing times (j) are very small (less than a minute). However, it is sensitive to the geometry (d).

Some measures of computing time and performance have been made for three-dimensional images with size N^3 for different values of N ($N = 8$, $N = 16$, $N = 32$, $N = 64$). They are detailed in [28].

– **Denton inversion formula**

This method is based on a generalization of the filtered backprojection formula which can be applied to 1D or 2D projections (parallel or divergent). This formula is adapted to the case of a 3D reconstruction from divergent projections by introducing some correcting factors. The detailed algorithm is described in [9].

Despite the fact that this method is theoretically applicable to 3D reconstruction (a), we have not found any practical development of this algorithm (h). Anyway, a very large number of views would be necessary so it is not a very interesting method for our case.

– **Backprojection filtering**

The method is inspired on the following theoretic result: the weighted (filtered) backprojection of the projections $\mathbf{B}'p$ is equal to a three-dimensional convolution of the image with the core $1/r^2$. The weighting factor of the backprojection is the ratio between the rotation source-center distance and the source-current point distance ([29], [13] and [2]). See Section 2.2.2 and Appendix C.

In spite of all the advantages of this method (applicable to 3D reconstruction (*a*), robustness against additive Gaussian noise (*f*), very simple implementation (*g*), already used (*h*), low memory cost (*i*) and low computing time (*j*)), a lot of source-points (projections) are needed in a very specific geometry: the different views must be taken with the emitters placed on the surface of a imaginary sphere which center is in the object. That is why, this method can not be used in our specific problem.

– Fan multi-cut approach

The idea here is to express the problem as a sequence of 2D reconstructions by filtered backprojection. For doing this, the beam divergence is neglected, so we approach the conical beam to a set of parallel fan beams. Each plane of the 3D matrix is then reconstructed by the 2D filtered backprojection algorithm, adapted to the fan geometry.

This method is applicable to 3D (*a*) and it has already been used (*h*), but its usefulness is not very clear because, even if it is algorithmically very effective, it can only be used when divergence is very weak.

– TTR algorithm

The TTR (True Three-dimensional Reconstruction) method reorganizes the set of (divergent) conical projections in a set of (parallel) cylindrical projections, when the X-ray source trajectory is on the surface of a sphere. The parallel projections correspond to the extreme case of conical projections where the source-center distance tends to infinity. From 2D parallel projections, the image is obtained by backprojection of the 2D filtered projections.

This method has already been developed (*h*) and it consists in reorganizing the conical data and backprojecting the filtered projections. But, as most analytical methods, it needs a lot of source-points (projections) on the surface of a sphere.

– 3D reconstruction in conical geometry by backprojection filtering

This method is an empirical generalization of the 2D reconstruction algorithm in fan geometry, for the case of a circular acquisition trajectory of the X source ([12], [29], [13] and [2]). See Sections 2.2.2, 2.2.3 and Appendix C.

There is no doubt about it, if one analytical method should be chosen for our problem, this one is the best choice. Indeed, it is the most used method (*h*) and the resulting quality is very good. It is a 3D method (*a*) with a very simple implementation (*g*), very low memory cost (*i*) and it is the fastest method (*j*) among those which give good quality results.

– 3D reconstruction in conical geometry via the Radon transform

This method leans on a exact formula which links the X-ray transform, $\mathbf{X}f$, to the first derived of the Radon transform, $\mathbf{R}'f$. To find the original function f , it is just necessary to invert $\mathbf{R}'f$. Another solution is to use the Hilbert transform of this first derived, $\mathbf{H}\mathbf{R}'f$. But this imposes global filtering of the projections, whereas the first approach just uses local filtering. See [16] for a detailed description.

As the previous one, this method is conceived for being used in 3D (*a*). It has been already used for several applications (*b*) but it is not very interesting for our case because complete data and/or a circular trajectory are required. So this method is not adaptable to different geometries (*d*).

– Contour reconstruction in 3D X-ray CT

This method is related to local or Lambda tomography. The success of the method is based on the fact that Λf (found by applying the Laplacian Δ to the backprojected image) has jumps wherever f has (f is the searched distribution). The basic idea of Λ tomography is to replace the non-local filter (used in the filtered-backprojection algorithm) by a local filter, that is to say, a regularized differentiation. For more details see [23].

It can be used in three dimensions (*a*) and it produces a surface reconstruction, not volumetric (*b*), in short computing times (*j*). So, it detects only the contours for local tomography.

Conclusion

In a general way, the analytical methods assume by principle a complete acquisition trajectory and a sufficient number of data (large number of projections, good projection sampling). In these conditions, these methods give good results and are preferred to the others because of their speed. However, when we have either a small number of views or very noisy data, these algorithms produce images with a large number of artifacts, and they appear to be not very robust.

Among the analytical methods, the least heavy (*g*) and the most used one (*h*) is *filtered backprojection*. The *discrete filtered backprojection* is the most widespread method (*h*). These methods suppose a sufficient number of data (large number of projections, good sampling) and they are heavy (*i*) and convergence may not be assured when noise is present (*e*). As the number of projections we can acquire is very limited and the angle between projections is often restricted, we conclude that analytical methods are not adapted to our problem.

In general, we can say about this kind of methods that they have been already used (*h*) and they are quite fast in terms of computing time (*j*), which are good points for choosing them. However, since addition of *a priori* information (*c*) is very limited and

they are rigid with respect to the adaptability to different geometries (d) (which are two of the most important criteria), we have decided not to use this kind of method.

2.4.3 Algebraic methods

These methods are different from analytical methods because they take into account in their formalism the discrete characteristics of the data (the used sensors have a finite resolution). These data, noted p_j , can be written as follows:

$$p_j = R f(r, \theta)_j \quad (2.5)$$

where $(r, \theta)_j$ are respectively the distance and the directing vector associated to the measure j , and R is the Radon operator. j varies from 0 to m , where m is the total number of projection measures.

In addition, the object function $f(x, y, z)$ is decomposed on a finite basis of n functions of summable square $h_i(x, y, z)$:

$$f(x, y, z) = \sum_{i=1}^n f_i h_i(x, y, z) \quad (2.6)$$

Putting together Equations 2.5 and 2.6, we can obtain a linear relation that links the measures to the coefficients of f :

$$p_j = \sum_{i=1}^n f_i R h_i(r, \theta)_j, \quad j \text{ varying from } 1 \text{ to } m \quad (2.7)$$

The set of relations in Equation 2.7 can be written in the following matricial way:

$$\mathbf{p} = \mathbf{X} \mathbf{f} \quad (2.8)$$

where \mathbf{p} is the vector with the m components of the measures, \mathbf{f} is a vector with n components f_i , and \mathbf{X} is a $m \times n$ matrix whose coefficients X_{ij} are equal to:

$$X_{ij} = R h_i(r, \theta)_j \quad (2.9)$$

This expression means that X_{ij} is the measure of the projection number j of the basis function h_i .

So, the reconstruction of \mathbf{f} is reduced to the inversion of a linear system. However, a lot of difficulties appear for the direct resolution of this system:

- The number of variables and the number of data obtained is very high. For example, 512^2 in 2D tomography or 512^3 in 3D ([29]), or 800×640 in the application described in [17].

- The system is often badly conditioned and \mathbf{X} has very small singular values.
- Often, the system in 2.9 is not consistent in the real case, due to noise.
- The limited number of projections leads to an under-determined system. In order to avoid this ambiguity, it is necessary to add *a priori* information about the problem to process ([17]).

In spite of these disadvantages, the algebraic methods have some advantages compared to analytical methods:

- The formalism that is used is very general and, thus, it can be applied to all kinds of geometry, as, for instance, geometries with limited angle, divergent fan, 3D. . .
- These methods allow to take into account a number of physical phenomena by modifying the R operator associated to the Radon transform. So, we could take into account collimation or auto-absorption effects.
- In a general way, these methods allow the introduction of *a priori* information about the analyzed object and, also, about the recording system, using some operators of constraints.

The most used basis functions are those which indicate square pixels in 2D, that is to say, $h_i = 1$ in pixel i and 0 anywhere else, or cubic voxels in 3D (see Figure 2.3). This approximation is what we have done for our first tests (Section 4.2.1). As shown in Figure 2.3, each line of the matrix \mathbf{X} corresponds to a projection ray and the coefficient X_{ij} would represent the length of the intersection of the j th ray with the pixel (voxel) i , in a more advanced version; in our first approach, it is a binary value that indicates whether the pixel (voxel) i is “touched” by the j th ray. Anyway, the matrix \mathbf{X} is very sparse, because a projection ray “touches” a number of pixels (voxels) about k , where k is the number of pixels (voxels) in one dimension.

Tomographic reconstructions reduce to the inversion of the previous linear system. This inversion can be done by the classical inversion methods (generalized inversion) or regularization methods, to take into account the bad conditioning of the problem.

The algebraic methods more widely used are the methods of generalized inversion adapted to the particular shape of the Radon operator, and they are iterative due to the large number of the data.

One difficulty of the iterative methods is to find a stop criterion. Often, due to the bad conditioning of the system, the continuation of the iterations leads to very noisy results, and most of times the process is stopped after a few iterations, what is a sort of regularization of the inversion.

Some references we have consulted about algebraic methods are [17], [29], [3], [4], [36], [21], [28], [13], [26] and [2].

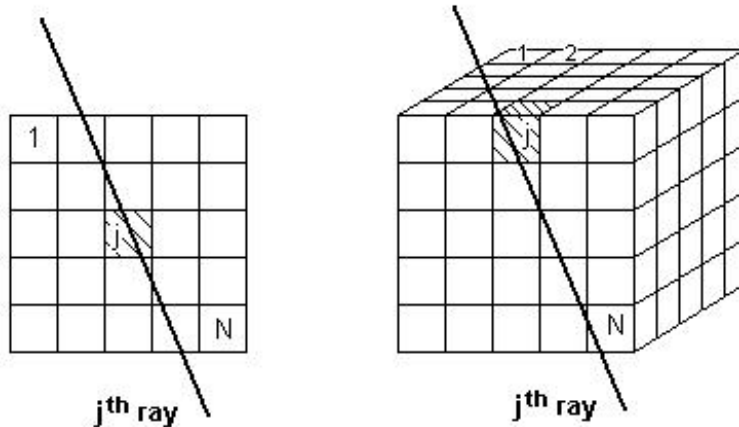


Figure 2.3: Discretization of f : a) in 2D, b) in 3D.

In the next paragraphs the existing algebraic methods are described:

– **ART (Algebraic Reconstruction Technique)**

The general idea of this method is already described above. ART is an iterative algorithm (to solve the linear system) which takes only one line of the matrix (see Equation 2.8) at the same time. In the basic version, the idea is to correct the solution at each iteration in order to make it consistent with the equation considered for this iteration.

The image is initialized as $\mathbf{f}^{(0)}$ (which may be zero or a uniform image). At each iteration k , an additive corrective term (which only depends on the j th equation) is added to the image $\mathbf{f}^{(k)}$. When the method is used without relaxation, this correction is calculated in order to fulfill the j th equation. This correction term can be interpreted as the backprojection of the difference between the measured projection and the calculated projection. The iteration $\mathbf{f}^{(k+1)}$ can be written matrixially as follows:

$$\mathbf{f}^{(k+1)} = \mathbf{f}^{(k)} + \lambda_k \frac{p_j - \mathbf{x}_j \mathbf{f}^{(k)}}{\|\mathbf{x}_j\|^2} \mathbf{x}_j^t \quad (2.10)$$

where $j = k(\text{mod } m) + 1$ (m is the number of components of the measures in \mathbf{p}), \mathbf{x}_j is the j th line of the matrix \mathbf{X} , $\|\mathbf{x}_j\|$ its Euclidean norm and λ_k a relaxation factor between 0 and 2 (see Equation 2.11). The relaxation factor λ_k can be interpreted as a weighting of the backprojection of the difference and it allows to accelerate the convergence.

This method is inspired on the Kaczmarz method. When $\lambda_k = 1$, it consists in doing a series of orthogonal projections on the hyperplanes associated to each equation. The algorithm converges towards the minimal norm (or least square) solution only if the system admits at least one solution, $\mathbf{f}^{(0)} = 0$ and λ_k varies in $[0, 2[$:

$$0 < \liminf_{k \rightarrow \infty} \lambda_k < \limsup_{k \rightarrow \infty} \lambda_k < 2 \quad (2.11)$$

This is the basic algorithm for algebraic methods. There are two versions: additive ART and multiplicative ART (see [2] for example). Additive ART converges towards the minimal norm solution and multiplicative ART can converge towards the maximum of entropy solution if the elements of \mathbf{X} take values in $[0, 1]$. This technique is very interesting as it is a compromise between the slow convergence of SIRT and the noise sensibility of ICM.

ART is applicable in 3D (*a*) and its first advantage is that *a priori* information can be introduced (*c*) in an easy way (regularization, for instance). This method is also adaptable to different geometries (*d*), easy to implement (*g*) and it has already been largely used (*h*) in two and three dimensions. It is a quite fast algorithm too (*j, k*), around 5 iterations could be sufficient. The disadvantage of this method is that it may not be stable in the presence of noise (*e*) but this can be controlled by stopping the iterations early enough. However, when data are noisy, a oscillation effect can be obtained, and there is no solution for this problem (*f*).

Lots of authors have used and described ART. See, for example: [18], [15], [29], [2], [3], [17], [36], [21], [28], [20], [13] or [26].

– SIRT (Simultaneous Iterative Reconstruction Technique)

This is an iterative method as ART but it works pixel by pixel instead of ray by ray. It converges to the minimal norm solution (in fact, it is a particular case of the least square minimization).

The principle of this method is that, at each pixel, all the projection measures corresponding to all the rays passing through this point are calculated and added. Then, a correction factor is applied to the density of this pixel. This factor is a function of the difference between the estimated projections and the measured projections:

$$\mathbf{f}_i^{(k)} = \mathbf{f}_i^{(k-1)} + \frac{\sum_{j \text{ passing through } i} \mathbf{p}_j}{\sum_{j \text{ passing through } i} \|\mathbf{x}_j\|} - \frac{\sum_{j \text{ passing through } i} \mathbf{x}_j \cdot \mathbf{f}^{(k-1)}}{\sum_{j \text{ passing through } i} n_j} \quad (2.12)$$

where $\|\mathbf{x}_j\|$ represents the length of the j th ray and n_j is the number of pixels crossed by this ray.

There is also a multiplicative way of applying the correction (see [29]).

The method starts with the initial estimate $\mathbf{f}^{(0)}$ which may be a uniform image or an image obtained by backprojection. The operation defined by Equation 2.12 (or the one for the multiplicative version) is repeated at each iteration. A relaxation factor could be introduced in order to assure a faster convergence.

As ART, it can be applied to 3D (*a*) but it is much slower than ART (an iteration of SIRT corresponds to M iterations of ART, where M is the number of measured projections). Addition of *a priori* information is easy (*c*) and it is adaptable to different geometries (*d*). Compared to the previous method, SIRT is very stable in the presence of noise (*e*) and more robust (*f*) than ART. The main disadvantage of this method is that memory cost (*i*) and computing time (*j*) are higher than for ART. With respect to the number of iterations (*k*), this method is also slower than ART.

Information about this method can be found in [29], [3], [17], [20], [21], [28], [13], [26] and [2].

– ICM (Iterated Conditional Mode)

In fact, this algorithm is a deterministic adaptation of the MAP (Maximum A Posteriori) (see Section 2.4.4 and Appendix D). The principle of this method is that, at each iteration, only the value of one site i is modified. That means that the minimization of the MAP criterion is only done compared to \mathbf{f}_i . Then, this algorithm converges to a local minimum of the energy of the MAP. If the initialization is good (relatively close to the searched solution), then the estimate will have a good quality and the convergence will be fast.

This method is well adapted to vascular networks reconstruction and largely used in Non Destructive Control and it does not converge necessarily to the minimal norm solution. The reconstructed image depends too much on the initialization for a medical application like ours, so we have found that it will be difficult to use such an algorithm in our case.

ICM can be used for 3D reconstruction (*a*), it is adaptable to different geometries (*d*) and it is possible to add some *a priori* information (*c*). The resulting images are quite contrasted, but this algorithm is sensitive to noise (*f*). In terms of computing time (*j*) and number of iterations (*k*), the ICM method is equivalent to ART.

For more details about ICM see [21], [2] or [26].

– SART (Simultaneous Algebraic Reconstruction Technique)

With this method only *one iteration* is needed to obtain good reconstruction results. To have a more precise reconstruction, the elements of the basis of f are chosen to be bilinear instead of canonical (as pixels and voxels are). This basis allows to calculate, at any moment, a continuous version of the function f to be reconstructed, whereas the canonical basis associated to the pixels or the voxels of the image just provides a discrete representation of f . Some correction terms are calculated by combining, at each iteration (associated to a particular projection) the corrections corresponding to all the rays of this projection. This is done to reduce more and more the inconsistencies with the real data of the projections (see [17], [21], [25], [20] and [36]).

SART is “the best” technique of the algebraic methods. It avoids the *aliasing* effect that can appear with ART. It is more robust against noise than ART (*f*) because it uses the average of the contributions of each projection ray. However, even if *a priori* information can be added (*c*), SART has a quite heavy implementation (*g*) and it consumes much more memory (*i*) than ART. Computing time (*j*) is higher than for ART too and this method is difficult to accelerate.

– **Natural pixels method (or Natural voxels decomposition with constraints)**

This method consist in developing the object function in a basis of functions adapted to the acquisition geometry, weighted by a weight function which translates the *a priori* informations ([13], [21] and [29]).

The objective of this method is to avoid too high computing time and memory cost and to reduce the interpolation effects. Its main advantage is that it reduces the reconstruction errors coming from traditional models of a square mesh.

The natural pixels method is applicable to different geometries (*d*) in three dimensions (*a*). A strong support constraint can be added, but it must be done carefully. Anyway, this algorithm does not need an additional regularization stage (*c*). It is a robust method (*f*) with good quality results and it is very stable in the presence of noise (*e*). The less restrictive is the constraint, the more the algorithm is stable. This method has already been developed (*h*) but the implementation is quite heavy (*g*) because the algorithm is complex and the modeling rigorous. However, the computing time (*j*) is low and a small number of iterations (*k*) is needed. The computing time with this method is directly proportional to M^2 (M is the number of views) while with the filtered backprojection method it is proportional to M .

– **ART by blocks**

This method is very similar to ART but the processing is done by blocks. Each block corresponds to a whole conical projection.

The system is partitioned as follows:

$$\begin{pmatrix} P_1 \\ \vdots \\ P_j \\ \vdots \\ P_M \end{pmatrix} = \begin{pmatrix} X_1 \\ \vdots \\ X_j \\ \vdots \\ X_M \end{pmatrix} f \quad (2.13)$$

where P_j represents one 2D conical projection (a vector $NP^2 \times 1$ if the 2D conical projection has a size of $NP \times NP$), X_j the corresponding projection matrix and M is the number of projections (compare with Equation 2.8).

A significant use of constraints (*c*) is necessary for this method to avoid instability (*e*) when data are noisy. This means that, with noisy data, ART by blocks is less robust than ART (*f*). However, this algorithm has already been developed (*h*) and the computing time (*j*) is better than for ART.

More information about this algorithm can be found in [11], [29], [28] and [2].

– Multi-resolution ART with support

The application of this method is for the reconstruction of highly contrasted objects. That is why, it is useful, for instance, for vascular structures. It needs the definition of a 3D region of support containing the object to be reconstructed, to bound the calculations in this region. The number of views necessary to obtain a good reconstruction varies from 6 to 15-20, depending on the vascular structure complexity.

This method has two different stages: first, the detection of the region of support containing the object of interest and next, the multiresolution estimation of the densities of the voxels in the region of support. More details about this method can be found in [33] and [39].

Addition of *a priori* information (*c*) is needed for this method, that has already been developed (*h*) with a good robustness against noise (*f*).

– Tomosynthesis by X-ray coded sources (Kaczmarz algorithm)

This method needs a special acquisition geometry called “code”: the X-ray sources are disposed in a same plane. The 3D volume is reconstructed slice by slice and the object is considered as a stack of slices with thickness zero:

$$f = \sum_{z=1}^N f_z \quad (2.14)$$

The reconstruction obtained with this algorithm is 3D but in slices (*a*), so we can say “half-3D”. Addition of *a priori* information (*c*) is possible. However, adaptability to different geometries (*d*) is limited. It has already been implemented (*h*) and only 4 or 5 iterations (*k*) are sufficient for convergence.

– Decomposition on cylindric basis functions

This algorithm was developed for the reconstruction of the thorax. The function *f*, with a limited support, is decomposed in a basis of functions generated in cylindrical coordinates, to better translate the shape of the object (the thorax). The basis functions are chosen so that their projections can be calculated analytically in the chosen geometry.

This method has already been developed (*h*) but the adaptation to different geometries (*d*) is difficult.

Conclusion

Since only a small number of views can be acquired in our case and acquisition angles are limited (criterion d), algebraic methods are well adapted, particularly because data are incomplete and irregularly distributed, but this fact implies that some regularization will be necessary. The most important advantage of algebraic methods is that *a priori* information about the object can be easily introduced (c) and implementation will not become too heavy (g). This information could be about the density, the support or the positivity and it will contribute to stabilization of the reconstruction process (c) and the improvement of the image quality. *Multiplicative methods* are specially appropriate when the number of projections is very small because they converge very quickly (k).

To sum up, we can say that most algebraic methods are adaptable to 3D processing (a), the conversion from pixels –2D– to voxels –3D– is often evident. The introduction of *a priori* informations (c) is possible and easy (iterative algorithms can be regularized by choosing a suitable number of iterations, for example). These methods are adaptable to different geometries (d) but their robustness against noise (f) is not specially good. Important memory costs (i) and high computing times (j) compared to analytical methods, are the price we have to pay for a simple implementation (g). The most important difficulty of these methods is the stop criterion for iterative methods: there can be convergence problems in the presence of noise (k).

2.4.4 Statistical methods

The algebraic methods applied to tomographic reconstruction allow to introduce some constraints about the obtained solutions and to take into account any type of acquisition geometry. Unfortunately, they converge, most of times, to a least squares solution, what implies a Gaussian noise on the data to guarantee robustness and allow to do only linear filtering or regularizations on \mathbf{f} .

The statistical methods take \mathbf{p} , and some times \mathbf{f} , as random variables with a law of probability that represents the uncertainty about the data (noise, modeling error) and about \mathbf{f} too (in the case of Bayesian models).

Historically, the statistical methods have been introduced in emission tomography to take into account Poisson noise. In these methods, data \mathbf{p}_i are considered as random variables, independent to each other, and distributed according to the law of Poisson $P(\mathbf{p}_i, \mathbf{f})$ of parameter $\bar{\mathbf{p}}_i(\mathbf{X}\mathbf{f})_i$, so:

$$P(\mathbf{p}_i, \mathbf{f}) = \frac{[(\mathbf{X}\mathbf{f})_i]^{\mathbf{p}_i} \exp[-(\mathbf{X}\mathbf{f})_i]}{\mathbf{p}_i!} \quad (2.15)$$

Shepp [35] took as a solution the distribution $\hat{\mathbf{f}}$ which maximized the law of probability $P(\mathbf{p}, \mathbf{f})$ so:

$$\hat{\mathbf{f}} = \max_{\mathbf{f}} \prod_{i=1}^M \frac{[(\mathbf{X}\mathbf{f})_i]^{\mathbf{p}_i} \exp[-(\mathbf{X}\mathbf{f})_i]}{\mathbf{p}_i!} \quad (2.16)$$

estimated with an EM (Expectation Maximization) algorithm. An adaptation of this method has been proposed for the transmission tomography.

The EM algorithm converges towards a local minimum of the probability and it is often very unstable. Thus, the iterative process is often stopped after some iterations to regularize the inversion.

A much more profitable approach is to use a Bayesian formulation, which allows to regularize by introducing some *a priori* information about \mathbf{f} . \mathbf{f} is then considered as a random field too, distributed according to the probability law $P(\mathbf{f})$.

We know $P(\mathbf{f})$ and the conditional probability $P(\mathbf{p}/\mathbf{f})$ given by the law of noise associated to the data, so the probability $P(\mathbf{f}/\mathbf{p})$ is obtained by the rule of Bayes:

$$P(\mathbf{f}/\mathbf{p}) = \frac{P(\mathbf{p}/\mathbf{f}) P(\mathbf{f})}{P(\mathbf{p})} \quad (2.17)$$

To find a single solution from this law of probability, some different estimators can be used. The more often employed is the MAP (Maximum A Posteriori), which maximizes $P(\mathbf{f}/\mathbf{p})$ (Appendix D).

The Bayesian methods used in tomography are different because of the considered noise model (Gaussian or of Poisson) and because of the shape of the *a priori* $P(\mathbf{f})$.

For more details about these methods see [29], [3], [4], [36], [17] and [13].

– Extended MENT (Maximum Entropy Tomography)

The MENT algorithm consists in finding the solution \mathbf{f} of the under-determined linear system that minimizes the criterion:

$$K(\mathbf{f}) = \iint_{\mathbb{R}^2} \mathbf{f}(x, y) \log(\mathbf{f}(x, y)) dx dy \quad (2.18)$$

This criterion comes from the information theory: the entropy of the solution must be maximized (Appendix E).

The *Extended MENT* algorithm consists in finding the solution \mathbf{f} of the under-determined linear system that minimizes the criterion:

$$K(\mathbf{f}, \mathbf{f}^*) = \iint_{\mathbb{R}^2} \mathbf{f}(x, y) \log\left(\frac{\mathbf{f}(x, y)}{e \cdot \mathbf{f}^*(x, y)}\right) dx dy \quad (2.19)$$

where e is the basis of the natural logarithm and \mathbf{f}^* represents the *a priori* about \mathbf{f} which is supposed to be positive and bounded. $\mathbf{f}^*(x, y)$ may be zero but, in that case, to obtain a criterion $K(\mathbf{f}, \mathbf{f}^*)$ finite, $\mathbf{f}(x, y)$ must be zero too. When no *a priori* information is available, we will take $\mathbf{f}^*(x, y) = e, \forall(x, y) \in \mathbb{R}^2$. In this case, the algorithm is reduced to MENT.

The criterion $K(\mathbf{f}, \mathbf{f}^*)$ is minimized with the technique of Lagrange multipliers.

This method is implemented in an iterative way. With *a priori* information, it produces better results than ART and it is very powerful with a limited number of projections.

This *a priori* information (c) is easier to introduce than in SART. Robustness against noise (g) is good but computing time (j) is very important and the implementation (g) is very heavy and complex.

To know more about this method see [17] and [21].

– Minimal variance estimator

For this method the functions \mathbf{f} and \mathbf{p} are considered as stochastic processes. The function \mathbf{f} must be found with the minimal variance estimator, taking into account as much as possible the geometrical properties of the acquisition system to factorize the equation system to invert.

The objective is to calculate the estimate $\hat{\mathbf{f}}$ that minimizes the mean of the square of the error of the estimation:

$$\hat{\mathbf{f}} = \min_{\mathbf{f}} E [(\mathbf{f} - \bar{\mathbf{f}})^t (\mathbf{f} - \bar{\mathbf{f}})] \quad (2.20)$$

Introduction of *a priori* information (c) is limited for this method but it can be interesting for some applications for it has already been developed (h).

– Bayesian estimation with maximal entropy *a priori*

This method is a Bayesian probabilistic approach in which the probability laws $P(\mathbf{f})$ (*a priori*) and $P(\mathbf{p}|\mathbf{f})$ (conditional) are attributed by using the maximum entropy method (ME). The chosen solution is obtained with the MAP criterion. The ME principle is only used to do the translation of *a priori* information about \mathbf{f} and \mathbf{N} (noise) in probability laws (Appendix E).

The discrete model used is:

$$\mathbf{p} = \mathbf{X} \mathbf{f} + \mathbf{N}$$

This method can be applied to 3D (a) in theory, but calculation cost may limit the practical application due to memory cost (i) and computing time (j) too high. However, this algorithm has already been used (h).

– 3D simulated annealing algorithm

This is a method of generalized optimization (Monte Carlo technique) which comes from statistical mechanics. Its more important advantage is that it allows to converge towards a global minimum.

The principle of this method tries to find the function \mathbf{f} that minimizes a cost function the following form:

$$\hat{\mathbf{f}} = \min [E(\mathbf{f}) = (1 - w)\|\mathbf{p} - \mathbf{X}\mathbf{f}\| + w\|\mathbf{f} - \bar{\mathbf{f}}\|] \quad (2.21)$$

where w is a real weighting coefficient, $\mathbf{X}\mathbf{f}$ represents the estimated projections, \mathbf{f} the researched 3D volume and $\bar{\mathbf{f}}$ the mean of the grey levels in a neighborhood.

The main advantage of this method is that it can be used with any acquisition geometry (d) and with a small number of views. It is applicable in 3D (a), the *a priori* information introduction (c) is very easy, it is robust against noise (f) and it has been developed (h). The disadvantage is that it is very slow, with high computing time cost (j).

– Reconstruction method introducing a Markovian model

The basis of this method is the classic ART method plus an iterative Bayesian method for the restauration of the 3D region of interest founded on a modeling by Markov fields. This algorithm is useful to reconstruct objects composed of several contrasted classes (materials). It is used for cases where a limited number of projections is available or when the acquisitions have a small signal to noise ratio ([10], [21], [29]).

The method is based on the description of the object by two fields: \mathbf{f} , the field of densities and λ , the field of labels that characterize the different classes. This Bayesian method has three steps:

- modeling of the formation of the projections: $P(\mathbf{p}/\mathbf{f}, \lambda)$,
- *a priori* modeling: $P(\mathbf{f}, \lambda)$,
- *a posteriori* distribution: $P(\mathbf{f}, \lambda/\mathbf{p})$ (obtained by the Bayes rule).

For this method the introduction of *a priori* information (c) is necessary (at least, locally). Other characteristics of this algorithm are its adaptability to different geometries (d) and its robustness against different kinds of noise (f). It has already been developed (h) but its computing time (j) is high even if the number of iterations (k) can be inferior to 5.

– **Adaptative algorithm for tomographic reconstruction preserving discontinuities**

The problem of tomography is modeled by the linear system $\mathbf{p} = \mathbf{X} \mathbf{f} + \mathbf{N}$. It is an ill-posed inverse problem (see Section 2.5 too). The regularization is obtained by modeling of the image to be reconstructed using Markov fields taking into account discontinuities. The image is calculated by minimizing the criterion:

$$J(\mathbf{f}) = \|\mathbf{p} - \mathbf{X} \mathbf{f}\|^2 + \sum_{i,j} \varphi((D_x \mathbf{f})_{i,j}) \sum_{i,j} \varphi((D_y \mathbf{f})_{i,j}) \quad (2.22)$$

where D is the gradient operator and φ is a regularization function. This equation illustrates the principle in a 2D case.

In fact, this is the type of method we have used for our work. But in this document it is considered as an algebraic method plus a regularization stage. Some descriptions of this algorithm can be also found in [6], [1] or [14]. For all the details about regularization see Chapter 3.

The 3D application (*a*) of this method is theoretically possible and it has already been tested (*h*) in 2D and in 3D ([34]). It is a robust algorithm against noise (*f*) and it is fast, with low computing times (*j*).

– **Estimation of simple or multiple objects from incomplete and noisy projections**

The object function \mathbf{f} is decomposed in J cylindric objects f_j on a continuous background f_b known *a priori*:

$$\mathbf{f}(x, y; z) = f_b(x, y; z) + \sum_{j=1}^J f_j(x, y; z) \quad (2.23)$$

For this method, the object is considered as a group of 2D cuts piled along an only skeleton, so it will not be a real 3D reconstruction (we will call it “half-3D” reconstruction) (*a*). However, it is a very robust algorithm (*f*) in the presence of noise and it has been developed in the case of a parallel geometry (*h*).

– **3D reconstruction of vessels from two angiograms by a Markovian approach**

The 3D contours of vessels are reconstructed slice by slice, from two digital angiograms acquired from perpendicular incidences. The object is considered as binary.

This method (described in [27]) has two stages:

- construction of a simple initial solution by stacking of ellipses,
- from this initial solution, reconstruction of sections (slices) cut by cut by minimization of a cost function (with the simulated annealing algorithm).

This algorithm produces a reconstruction in slices (“half-3D”) (*a*), some *a priori* informations can be added (*c*) and it has already been implemented (*h*).

Conclusion

Statistical methods have been developed in order to overcome the limits of algebraic methods: assumption of Gaussian noise. EM (Expectation Maximization) algorithms are instable (*e*), so a Bayesian formulation was developed. However, the stochastic methods, although they seem theoretically attractive, do not lead in general to images of a quality which would justify their complexity. That is to say, stochastic methods are very complex to implement (*g*) and they are not much more powerful than deterministic methods. And, in fact, the Gaussian hypothesis is often conserved.

The main characteristics of statistical methods are that they need *a priori* information addition (*c*), which would be quite simple, they are very efficient and robust against noise (*f*) but their implementation cost (*g*) is very high.

2.4.5 Structural methods

Finally, the last group corresponds to “structural methods”. Here, only the “structures” of the objects of interest are searched; for instance, a set of points, some contours or some surfaces will be reconstructed. This is why they are not really adapted to volumetric reconstructions (*b*). These methods use most often some geometrical considerations, techniques from the graph theory or some approaches inspired from artificial vision ([3], [29]).

– Tomographic reconstruction using geometrical methods

Geometrical methods try to reconstruct directly the surface of the examined objects and not a 2D or 3D image of the absorption coefficients.

The principle consists in extracting directly the contours of the object in the sinogram². The contours are converted in reconstructed curves or surfaces, in the real space, by the geometrical methods.

When the objects to reconstruct are well contrasted and with a quite convex section, these methods allow to obtain this contour reconstruction (2D curves or 3D surfaces). For more details see [37].

This method is easily applicable to 3D sinograms (*a*). According to [29], it has only been developed in 2D but not in 3D (*g*). Anyway, this algorithm is not interesting for our case because it gives only a surface reconstruction (*b*).

²Sinogram: image formed by the set of successive lines of acquisition of the scanner X

– **Reconstruction of ventricles and arteries from two orthogonal projections by using the method of the median curve**

This method reconstructs 2D binary cuts from their two 1D densitometric profiles and from the median curve. The images are supposed not to be very noisy. There are two steps:

- determination of the median curve;
- refinement of the solution by an optimization method (minimal norm function).

For this method, the sections to be reconstructed must be connected, without a hole and regular.

The resulting images are 2D binary slices (*a*), a preprocessing is needed to avoid problems with respect to robustness against noise (*f*) and it has already been developed (*h*).

– **3D reconstruction of an element of the jaw from two orthogonal X-ray radiographies**

From two 1D densitometric profiles this method tries to furnish the corresponding 2D section. The density profiles must be known *a priori* and the noise is supposed to be of Poisson. There are two different steps:

- the starting point is an approximative reconstruction (initial flood solution);
- refinement of the solution by an optimization method (maximal flood at minimal cost).

This algorithm assumes that the objects to be reconstructed have connected sections without a hole. The resulting images are 2D binary sections obtained from 1D profiles. This is why, although the application is very close to ours, we cannot use this method in our case.

This method has already been tested (*h*) and further research works are described in [30].

– **Space-time vascular reconstruction in computer vision**

These are some methods that introduce constraints by symbolic modeling, by adding a third view or by estimating the movement, for any geometry.

These methods have also been tested (*h*) and their advantage is that they are adaptable to different geometries (*d*).

Conclusion

The advantage of the structural methods is that it is possible to introduce *a priori* information (*c*). They find their main application field in vascular imagery, so often the reconstruction is not volumetric but binary (*b*).

However, even if they are not very useful for volumetric reconstruction in our case, it could be a good idea to use structural methods to reconstruct specifically some objects (as the dental canal, for instance) and then add these constraints to the volumetric reconstruction.

2.4.6 Other methods

We have found two other reconstruction methods used in medical applications. However, these methods are not suitable for our case as they provide only a surface reconstruction. These methods are:

- *Stereovision*: two different points of view of the three-dimensional object allow to calculate a 3D reconstruction (see [4]);
- *Echography*: ultrasounds allow to obtain a 3D image of the object surface (see [31] and [32]).

2.5 Choice of the method

The possibility of adding *a priori* information (criterion *c*) and adaptability to different geometries (*d*) are absolutely necessary for our reconstruction problem. This is difficult to incorporate in analytical methods. So, despite their good behavior in terms of computing time (*j*) and the fact that they are already largely used for similar applications (*h*), we have not chosen them to develop our work.

On the other hand, although statistical methods are more stable (*e*) and more robust against noise (*f*) than the other kinds of methods, they are often very complex to implement (*g*) for a resulting quality not as good as it could be expected. As we had some constraints of time, due to the fact that we had to finish a first version of the software quite quickly, the criterion about implementation complexity (*g*) became a priority.

Finally, structural methods are mainly useful for binary reconstructions (*b*). So, they are not adapted to our specific case.

Therefore, we have chosen algebraic methods because they allow to introduce easily *a priori* information (*c*) without having a very heavy implementation (*g*) and they are adaptable to different geometries (*d*). The disadvantages of this kind of methods are that their computing times (*j*) and memory costs (*i*) are a little high and that they are not very robust against noise (*f*). This will lead us to introduce regularization constraints.

Among the algebraic methods, ART (Algebraic Reconstruction Technique) and SIRT (Simultaneous Iterative Reconstruction Technique) seem to be the more appropriate candidates due to their simplicity for introducing the *a priori* information (*c*) and for implementing the algorithm (*g*).

Equation 2.24 expresses the problem to be inverted, where \mathbf{p} represents the projection data, \mathbf{f} is the object to be reconstructed, \mathbf{X} is the projection matrix and \mathbf{N} represents data noise. The algebraic method principle is shown in the right term of the equation, where k is the iteration number and λ is a relaxation coefficient.

$$\mathbf{p} = \mathbf{X} \mathbf{f} + \mathbf{N} \Rightarrow \mathbf{f}^{(k+1)} = \mathbf{f}^{(k)} + \lambda \mathbf{X}^T (\mathbf{p} - \mathbf{X} \mathbf{f}^{(k)}) \quad (2.24)$$

SIRT provides a better robustness against noise (*f*) and is more stable (*e*) than ART. That is why we preferred to use SIRT.

However, the consequence of choosing algebraic methods is that an additional stage must be developed to compensate the disadvantage of having incomplete data. The next step, described in Chapter 3, is regularization.

Chapter 3

Regularized reconstruction

As we have shown in Chapter 2, the most suitable reconstruction methods for our problem (described in Chapter 1) are algebraic methods. Among them, ART and SIRT are the best methods with respect to the criteria described in Section 2.3. However, as the data are very incomplete, it will be necessary to constraint the possible solutions to find the one that corresponds the best to our specific case. These constraints can be added thanks to a regularization stage.

The regularization principle and the different existing methods are detailed in this chapter. The choice of the most appropriate regularization method to our problem is discussed in Section 3.2.

3.1 Regularization principle

The algebraic methods we have chosen for reconstruction are iterative methods. Such methods allow to avoid the inversion of big matrices and to introduce other constraints or other stabilizing functions (linear or not).

In order to mitigate the ill-posed character of our problem of reconstruction, a set of solutions is searched such that they “almost fulfill” the direct problem $\mathbf{p} = \mathbf{X}\mathbf{f}$ (Equation 2.8) and then the solution that minimizes a “regularity” criterion will be chosen.

In practice, this means that a criterion must be minimized:

- either a criterion of the form $J = J_d + J_r$ where J_d is a term of fidelity with the data (for example $J_d = \|\mathbf{p} - \mathbf{X}\mathbf{f}\|^2$) and J_r is a regularization term;
- or a criterion J_c under the constraint $\|\mathbf{p} - \mathbf{X}\mathbf{f}\|^2 \leq \epsilon^2$ with a small ϵ .

The optimization under constraint J_c is more powerful because it allows a better control of the difference with the data; however, it often implies the use of techniques which are heavy not only from an algorithmical point of view, but also from a computing time point of view.

Preserving discontinuities

The choice of the regularization method depends on the application where it will be used. In our case, the preservation of discontinuities is the main characteristic to be fulfilled, as in our medical images the most important features to obtain with detail are the contrasted parts: dental canal, limits of the jaw...

Regularization preserving discontinuities means that the image will be smoothed but the sharp edges will be respected.

The term J_r can be expressed in a general way as follows:

$$J_r = \sum_{\text{voxels}} \phi(\Delta_i\{x\}) + \phi(\Delta_j\{y\}) + \phi(\Delta_k\{z\}) \quad (3.1)$$

where Δ_i , Δ_j and Δ_k represent the operators of difference between neighbors for each direction of the space (in 3D) and ϕ is a potential function.

The energy function

The approach of the regularization preserving the discontinuities often consists in searching the minimum of an energy function with the characteristics shown above. The purpose of the regularization step is to limit the solution domain by introducing information about the object to reconstruct through the minimization of an energy function:

$$J = J_d + J_r = Q + \lambda \cdot \Psi \quad (3.2)$$

where, applied to our case:

- The first term ($J_d = Q$) constrains the solution to have projections as close as possible to the original ones. It is the *fidelity to the data* term and it is expressed as:

$$J_d = Q = \|\mathbf{p} - \mathbf{X}\mathbf{f}\|^2 \quad (3.3)$$

To minimize this term means to minimize the difference (in form of quadratic error) between the reconstructed image and the data.

- The second term ($J_r = \lambda \cdot \Psi$) models *a priori* knowledge about the object, as positivity of the values, homogeneity of the volume, contrast... It is the *regularization* term.
- λ is the parameter that controls the regularization weight compared to the projection information.

3.2 Choice of the regularization term

3.2.1 Adaptation to ART methods

As we have shown in Chapter 2 and in Section 3.1, the principle of ART methods is to minimize this function:

$$J_{ART}(\mathbf{f}) = \|\mathbf{p} - \mathbf{X}\mathbf{f}\|^2 \quad (3.4)$$

This function corresponds to the *fidelity to the data* term (Q) of the energy function (see Equations 3.2 and 3.3). This error function is quadratic and the ART solution is:

$$\hat{\mathbf{f}} = \arg \min_{\mathbf{f}} J_{ART}(\mathbf{f}) \quad (3.5)$$

The minimization of equation 3.4 by an ART-type algorithm is done in an iterative way:

$$\mathbf{f}^{k+1} = \mathbf{f}^k + \lambda_k r_k \quad (3.6)$$

where λ_k is a relaxation parameter and r_k is the correction term added to $\mathbf{f}^{(k)}$ at each iteration. This has been shown in detail in Equation 2.10.

Therefore, we can deduce that the implementation of an ART method for reconstruction (Equation 3.4) will be easily adapted to add the regularization step (Equation 3.8), including the positivity and the *a priori* constraints. This is why, we decided to use this method (which is also described in detail in [2]) for the regularization stage.

3.2.2 The potential function

The *potential function* ϕ , which characterizes the *regularization* term itself, should be convex to guarantee the convergence of iterative optimization algorithms towards the global optimum (as detailed in [34]) and it defines the homogeneity and contrast of the volume to reconstruct. As we have already shown, in our specific case, discontinuity preservation is needed.

The choice of the potential function ϕ is a very delicate problem which has already been studied by a lot of authors. A discussion about the potential function to choose is done in [34]. Here it is shown that the quadratic regularization function (introduced by *Tikhonov* [38]) of the form $\phi(x) = \|\Delta x\|^2$ (where Δ is the operator of differences between neighbors) is not very suitable for a case like ours, as this function allows to smooth the noise present in the image but it smoothes indifferently the homogeneous zones and the sharp contours. Other approaches avoid this low-pass filtering locally at edges (to preserve discontinuities) by using the Tikhonov function (see Table 3.1) near the origin but truncating it when we have larger differences between neighbors (edges zones). Later, some more regular functions have been proposed. However, as they were not convex, the

research of the optimum is more difficult. Finally, a classification of functions has been done [22]. Among the different kinds of functions the convex, not bounded, with bounded derivative functions seem to be the best adapted to the preservation of discontinuities. The function of *Huber* [19] and the “minimal surfaces” (*Charbonnier* [5]) function belong to this class and they have been used as regularization functions (see Table 3.1). For these reasons, we have decided to use them to implement our regularization algorithm.

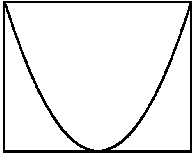
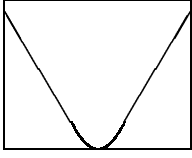
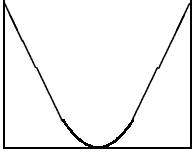
Function	Appearance	Discontinuity preservation
Tikhonov $\phi(x) = x^2$		Bad
“Minimal surfaces” Charbonnier $\phi(x) = \sqrt{1 + x^2} - 1$		Medium
Huber $\phi(x) = \begin{cases} x^2 & \text{if } x \leq \alpha \\ 2 \cdot \alpha \cdot x - \alpha^2 & \text{if } x > \alpha \end{cases}$		Medium

Table 3.1: Convex potential functions.

Among the selected functions, we have chosen *Huber*’s one to implement the algorithm because it gives us an additional parameter to play with in order to obtain the best reconstruction. The parameter α is an adjustment parameter of the function. If α decreases, the *Huber* function will become closer to the “V” function and, therefore, the edges of the image will be more respected. On the contrary, if α increases, the *Huber* function will become closer to the *Tikhonov* (pure quadratic) function and the edges of the image will be smoother. See Figure 3.1.

3.2.3 The positivity term

As the resulting volume must have only positive values (grey level intensities), a *positivity constraint* has to be added. It will be described by the following expression:

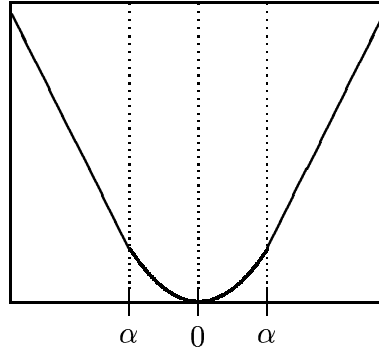


Figure 3.1: The parameter α in the Huber function

$$\mathcal{K}f_{i,j,k} = \begin{cases} f_{i,j,k} & \text{if } f_{i,j,k} < 0 \\ 0 & \text{otherwise} \end{cases} \quad (3.7)$$

Minimizing $\|\mathcal{K}f\|^2$ implies to minimize the negative values of the reconstructed image f . This can be interpreted as a first part of the *regularization* term (as shown in Equation 3.8).

3.2.4 The energy function to minimize

Thus, the entire energy function to minimize in our case is:

$$\begin{aligned} J(f) = & \underbrace{\|\mathbf{p} - \mathbf{X}f\|^2}_{\text{Fidelity to the data}} + \underbrace{\|\mathcal{K}f\|^2}_{\text{Positivity}} + \lambda^2 \sum_{i,j,k} \phi(f_{i,j,k} - f_{i-1,j,k}) + \\ & + \lambda^2 \sum_{i,j,k} \phi(f_{i,j,k} - f_{i,j-1,k}) + \\ & + \underbrace{\lambda^2 \sum_{i,j,k} \phi(f_{i,j,k} - f_{i,j,k-1})}_{\text{a priori}} \end{aligned} \quad (3.8)$$

The regularization functions that participate in the energy function and that allow to preserve discontinuities (while ensuring the convexity of the energy function) are non-linear and some iterative methods must be used to minimize the energy function. This is described in Section 3.3.

3.3 Optimization method

The energy function in Equation 3.8 takes into account both the reconstruction method (ART-type) and the regularization term (positivity included). Once we have defined completely this energy function, the next step is to minimize it.

About convexity

It is important to outline that we are looking for global convergence (towards a global minimum for any initialization). This is why, it is not trivial to minimize $J(\mathbf{f})$ because, in general, it may be non-convex and, in this case, there could be some local minima. The two first terms of Equation 3.8 are convex but the third one not always. It depends on the choice of the potential function ϕ as it has already been discussed in the previous sections and in [2].

Theoretically, a non-convex function ϕ furnishes better results than a convex function because it penalizes less the strong edges. However, the optimization part will become more difficult to solve in the case of a non-convex function. In this context, the deterministic algorithms (described in next paragraphs) provide generally a solution corresponding to a local minimum of the function and the quality of the solution depends on the initialization.

Thus, as it is discussed in the previous section, we have chosen a convex potential function. And so, the use of the deterministic methods is not a problem and we will obtain a global minimum.

Families of optimization methods

Two main families of methods exist to perform the optimization stage: stochastic methods and deterministic methods. The choice of the optimization method depends on the nature of the energy function to minimize.

- Stochastic methods are inspired by the annealing process used in metallurgy: after having heated the material to a very high temperature, one lets it very slowly cool (this is called *relaxation* in reconstruction) in order to obtain a perfect crystallization. Two different algorithms are used: the *simulated annealing with Metropolis dynamics* and the *Gibbs sampler*. The former is described in detail in [2]. Minimization with this kind of methods implies too high computing times for medical applications. For this reason, we have not used this kind of methods.
- Deterministic methods. The main algorithms are:
 - *Conjugate Gradient Algorithm*
 - *Iterated Conditional Modes (ICM)*
 - *Gradual Non-Convexity (GNC)*
 - *Semi-quadratic minimization*

The details about this family of optimization methods can be found in [34] and [2].

Our choice

The *semi-quadratic minimization* algorithm has been chosen for our implementation because this method provides convergence towards a global minimum in the case of a potential function ϕ which is not convex and with the constraint of a sparse matrix (X) (see Sections 2.4.3 and 4.2). Moreover, this algorithm does not depend on the initialization, which is very convenient for a medical application.

For the study of this minimization technique, we start with a more general formulation of the function $J(\mathbf{f})$ in Equation 3.8:

$$J(\mathbf{f}) = Q(\mathbf{f}) + \lambda^2 \sum_{m=0}^{M-1} \Phi[V_m(\mathbf{f})] \quad (3.9)$$

where Q and V_m are two convex functions, and Φ is a strictly concave function. Delaney and Bresler [8] have proposed a minimization algorithm for this kind of function, the “ \mathcal{M} algorithm”. This algorithm is described briefly in Appendix F.

In the particular case of choosing:

$$Q(\mathbf{f}) = \|\mathbf{p} - \mathbf{X}\mathbf{f}\|^2 \quad (3.10)$$

$$V_m(\mathbf{f}) = [\mathcal{D}]_m^2 \quad (3.11)$$

$$\Phi(t) = \phi(\sqrt{t}) \quad (3.12)$$

the function 3.8 is found because $\Phi(V_m(\mathbf{f})) = \phi([\mathcal{D}]_m)$ where \mathcal{D} represents the operator of differences between neighbors (\mathcal{D}_x , \mathcal{D}_y and \mathcal{D}_z will be the differences between neighbors for each direction of the space). The convergence of the \mathcal{M} algorithm is demonstrated in a general case. Function 3.8 is just a particular case.

In addition, it can be seen that:

$$\Phi'(t) = \frac{\phi'(t)}{2\sqrt{t}}$$

and so, the algorithm of semi-quadratic regularization described by Charbonnier [5] is found. We describe here this algorithm to show the link with the \mathcal{M} algorithm and, thus, its convergence properties. The method proposed by Charbonnier is based on the transformation of the function 3.8 in a dual semi-quadratic function using an auxiliary variable, b . Taking as a base the theorem of Geman and Reynolds [14] extended by Charbonnier [7], Equation 3.9 (or more particularly Equation 3.8) can be rewritten in the following way:

$$\begin{aligned}
J^*(\mathbf{f}) = & \|\mathbf{p} - \mathbf{X}\mathbf{f}\|^2 + \|\mathcal{K}\mathbf{f}\|^2 + \lambda^2 \sum_{i,j,k} \left\{ (b_x)_{i,j,k} (\mathcal{D}_x \mathbf{f})_{i,j,k}^2 + \psi[(b_x)_{i,j,k}] \right\} + \\
& + \lambda^2 \sum_{i,j,k} \left\{ (b_y)_{i,j,k} (\mathcal{D}_y \mathbf{f})_{i,j,k}^2 + \psi[(b_y)_{i,j,k}] \right\} + \\
& + \lambda^2 \sum_{i,j,k} \left\{ (b_z)_{i,j,k} (\mathcal{D}_z \mathbf{f})_{i,j,k}^2 + \psi[(b_z)_{i,j,k}] \right\}
\end{aligned}$$

where ψ is a strictly convex and decreasing function.

The following property can be observed: if b_x , b_y and b_z are fixed then the criterion $J^*(\mathbf{f})$ is quadratic in \mathbf{f} . If \mathbf{f} is fixed, the criterion is convex in b and we can obtain analytically its minimum (see the extended theorem of Geman and Reynolds in [7] or in [2]). This interpretation leads to the ARTUR algorithm which uses successive minimizations, first in \mathbf{f} , then in b .

$$b_{i,j,k}^{k+1} = \frac{\phi'([\mathcal{D}\mathbf{f}]_{i,j,k})}{2[\mathcal{D}\mathbf{f}]_{i,j,k}^2}, \quad (i, j, k) = 0, 1, \dots, N-1 \quad (3.13)$$

$$\mathbf{f}^{k+1} = \arg \min_{\mathbf{f}} \left\{ \|\mathbf{p} - \mathbf{X}\mathbf{f}\|^2 + \lambda^2 \sum_{i,j,k} b_{i,j,k}^{k+1} [\mathcal{D}\mathbf{f}]_{i,j,k}^2 \right\} \quad (3.14)$$

where N is the size of each dimension of the volume \mathbf{f} (we suppose a cubic volume) and the parameter λ represents the weight of the fidelity to the data term compared to the *a priori*.

These steps are repeated until a stop criterion. Appendix G presents the different calculation stages in the case of choosing a gradient descent method to minimize Equation 3.14. This is inspired by the implementation described in [2] but here we have an adaptation to the 3D case.

The algorithm LEGEND, which uses a semi-quadratic regularization too, is described in [34] and it is compared to ARTUR. However, we have chosen the latter, because of its proximity to the ART reconstruction method. It is just necessary to “add” a term of weighed smoothing (see Appendix G). In addition to the convergence advantages, this algorithm is also interesting from a point of view of the computer implementation.

A description of the complete implementation and a comparison of the obtained results depending on different parameters are described in the next chapter.

Chapter 4

3D regularized reconstruction from a small number of projections in maxillo-facial imaging: feasibility and first experimental results

We have concluded that regularized algebraic methods are the best choice for our problem. In this chapter we describe the simulator we have used to do our tests (with parallel projections as a first approach) in Section 4.1, the regularized reconstruction implementation in Sections 4.2 and Appendix H, and next we describe the tests we have done and why in Section 4.3. Finally we draw some conclusions in Section 4.4 from the obtained results (described in Section 4.3). Preliminary results have been published in [24].

4.1 Simulator

In this section, we describe a simulator which aims at computing projections from a complete 3D volume simulating the dental acquisitions. These projections will serve to evaluate our reconstruction method.

4.1.1 Available data

For the simulation stage, we use CT scanner data from which we simulate radiographic acquisitions. These data are three-dimensional images coded on 16 bits (one sign bit included). Their dimensions are typically $512 \times 512 \times Z$ where Z is not fixed but is around 100 slices. The pixel size for each slice is $0.24 \text{ mm} \times 0.24 \text{ mm}$, and the space between slices is 0.5 mm. However, the slice thickness is 0.63 mm so that there is an overlapping of 0.13 mm between neighbor slices. This makes a scanner exam have a size of approximately 50 MB. These images can be converted to a 8 bit format (that is to say, values from 0 to 255 for grey levels), which would reduce the size to 25 MB for each exam. This is very useful to reduce processing time and memory costs.

4.1.2 The objective of the simulator

The objective of the simulator is to produce several 2D images that represent the radiographic projection of some region of interest in the scanner exam volume. It is very important for the reconstruction process to control the number and the geometry of these projections (do not forget that we assume parallel projections as described in Section 2.2.3). The resulting images will have a specific resolution (assuming square pixels) that could be introduced as a parameter in the simulator interface. Other parameters to be introduced are the distance between the sensor and the emitter, and the dimensions of the image (height and width in millimeters), which will be equal to the emitter and sensor surface dimensions for simplicity. The interface is described in Section 4.1.4.

4.1.3 System geometry

The system geometry is defined by two reference systems: one is an absolute coordinate system defined by the scanner data and the other is a relative coordinate system related to each acquisition (in the projection plane). These two coordinate systems are described in the next paragraphs.

Absolute coordinate system

The absolute coordinate system takes the origin of the scanner volume in the upper front right corner of the cube containing the data, as shown in Figure 4.1. The x axis goes backwards from the front part of the mandible to the back, the y axis goes from right to left (right and left being related to the usual anatomical orientation) and the z axis from top to bottom.

We have chosen such a coordinate system because of the DICOM format (which increases the slice coordinate from top to bottom) and in order to have a direct coordinate system, so we can use classic operations (scalar and vectorial products, for instance) without redefining them.

An example of the coordinate system on a real scanner exam is shown in Figure 4.2.

Relative coordinate system

Thanks to the navigation system we will be able to locate precisely the position of the sensor and of the emitter for each radiographic projection (Chapter 1). This defines a parallelepiped placed somewhere in the data volume, as we suppose that the sensor and the emitter have the same size and are perfectly aligned (they are on parallel planes, and their equivalent edges are on the same plane perpendicular to the sensor plane). This is illustrated in Figure 4.3.

To work more easily on the projection plane (or sensor plane) we have defined a coordinate system relative to each projection parallelepiped. The origin will be located in the

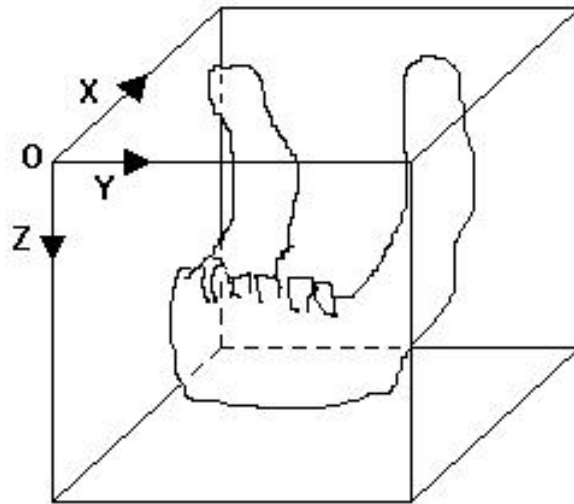


Figure 4.1: Absolute coordinate system.

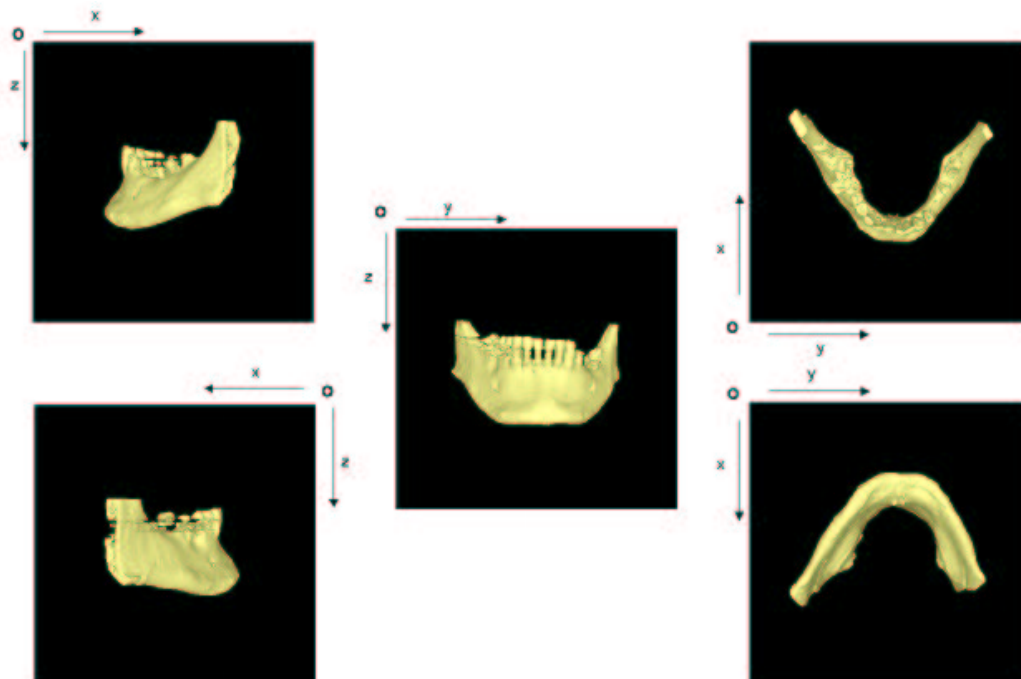


Figure 4.2: An example of the absolute coordinate system from different points of view. From top to bottom and from left to right: view from the left side, view from the right side, front view, upper view, bottom view.

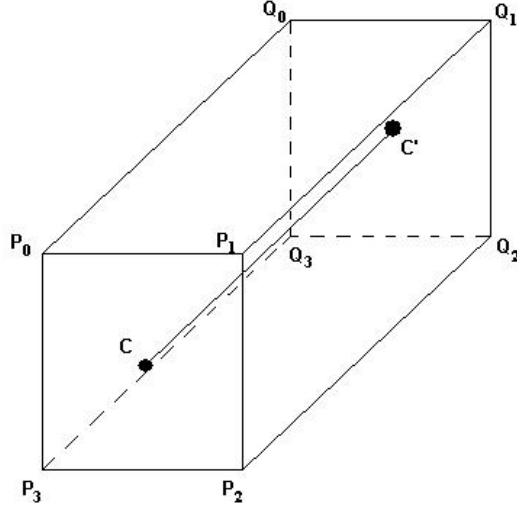


Figure 4.3: Parallelepiped defined by the sensor and the emitter: P_0, P_1, P_2, P_3 (the sensor corners) and C (the sensor center) define the sensor or projection plane; Q_0, Q_1, Q_2, Q_3 (the emitter corners) and C' (the emitter center) define the emitter plane.

upper left side of the rectangle placed in the sensor plane (P_0). Here, we will rename the coordinates as follows: S (the *Side* vector) is equivalent to the x axis, T (the *Top-bottom* vector) is equivalent to the y axis, and N (the *Normal*) is equivalent to the z axis. This is shown in Figure 4.4. In this figure, points P_0, P_1, P_2 and P_3 are on the sensor plane, and their equivalent points on the emitter plane are Q_0, Q_1, Q_2 and Q_3 .

So, the relative coordinate system will be placed differently for every projection.

4.1.4 Interface

The simulator interface is shown in Figure 4.5. We can see that the required parameters for each projection are the following:

- The *Depth* (D) of the projection, that is to say the distance between the sensor plane and the emitter plane (which are parallel).
- x_0, y_0, z_0 , coordinates of the relative coordinate system origin (P_0) on the sensor plane (*Position*).
- x_N, y_N, z_N , coordinates of the *Normal* (N) to the sensor plane.

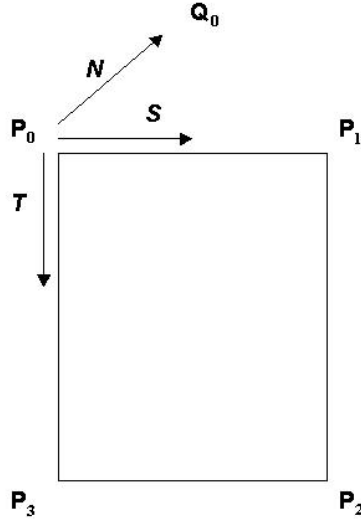


Figure 4.4: Relative coordinate system diagram.

- The size of the projection images we want to obtain (*Height* – PH – and *Width* – PW –).
- The resolution (*Pixel Size* – PS –) of the resulting 2D images (we will obtain square pixels).
- x_T, y_T, z_T , coordinates of the *top-bottom* vector (T) of the sensor plane. The *Check* button tests “Normal – Top-bottom direction” orthogonality.

The units for all parameters are millimeters (mm).

4.1.5 Geometrical construction

From parameters introduced in the interface, all necessary points and vectors to define the parallelepiped can be calculated. Before describing these calculations in detail, we remember that a plane can be defined by a point and its normal (a, b, c) , and its equation is:

$$ax + by + cz = d \quad (4.1)$$

Here are the detailed steps we have followed to define the parallelepiped:

- The sensor plane is already defined with point P_0 and vector $N(x_N, y_N, z_N)$.
- The emitter plane can be found with point Q_0 and normal N (or its unitary vector):

$$Q_0 = P_0 + D \cdot \frac{N}{|N|}$$

where $|N| = \sqrt{x_N^2 + y_N^2 + z_N^2}$

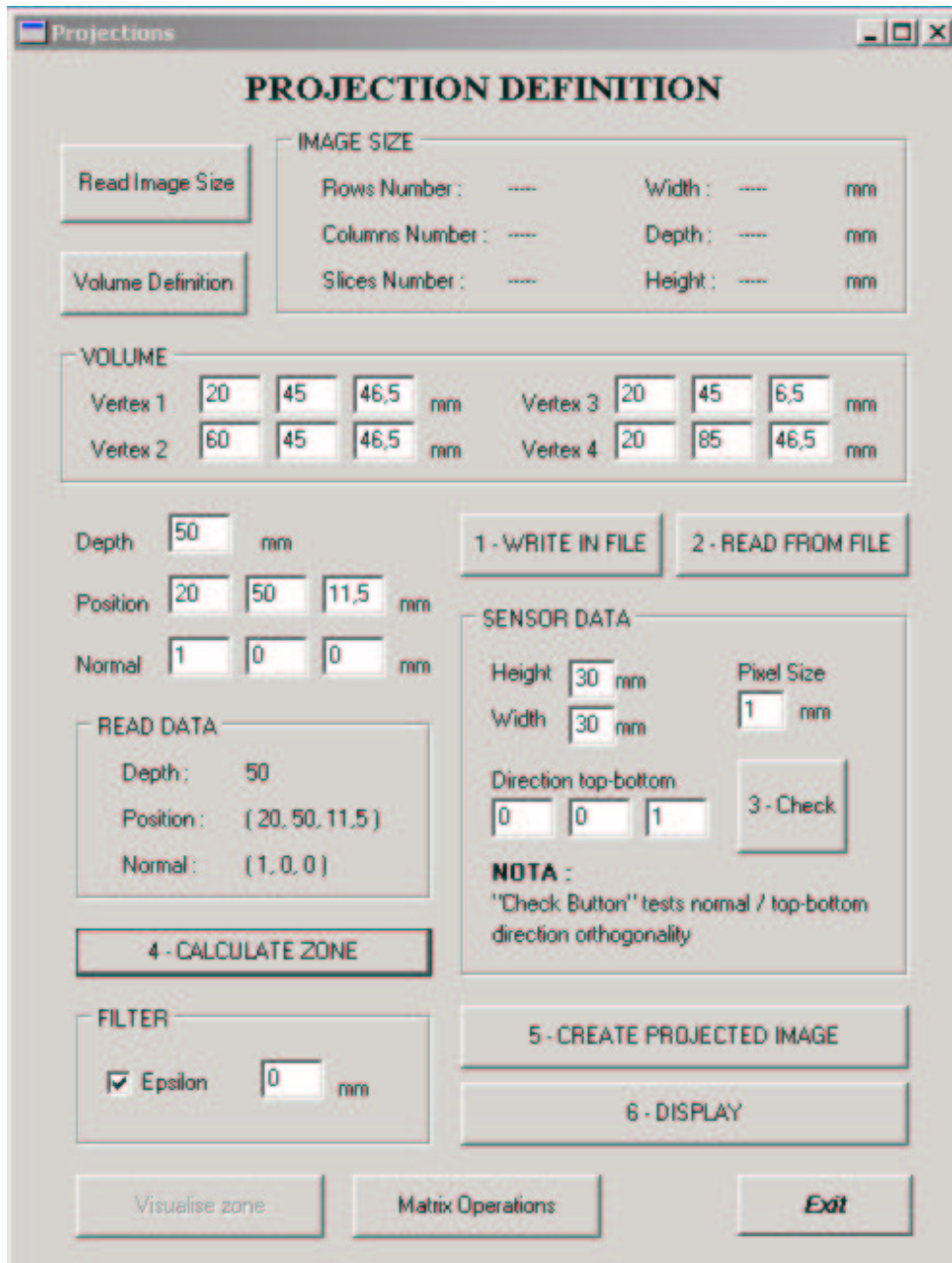


Figure 4.5: The simulator interface.

and D is the projection depth.

- The top plane is defined by point P_0 and vector $T(x_T, y_T, z_T)$ (or its unitary vector) with:

$$|T| = \sqrt{x_T^2 + y_T^2 + z_T^2}$$

- For the bottom plane we will use vector T and point P_3 :

$$P_3 = P_0 + PH \cdot \frac{T}{|T|}$$

where PH is the projection height in mm.

- The left side plane will be calculated with point P_0 and vector $S(x_S, y_S, z_S)$ which is found from the vectorial product $T \times N$:

$$\begin{aligned} S &= T \times N = (x_T, y_T, z_T) \times (x_N, y_N, z_N) = \\ &= (y_T \cdot z_N - z_T \cdot y_N, z_T \cdot x_N - x_T \cdot z_N, x_T \cdot y_N - y_T \cdot x_N) = (x_S, y_S, z_S) \end{aligned}$$

$$\text{and } |S| = \sqrt{x_S^2 + y_S^2 + z_S^2}$$

- For the right side plane we will use the same vector S and the point P_1 :

$$P_1 = P_0 + PW \cdot \frac{S}{|S|}$$

where PW is the projection width in mm.

4.1.6 Projection implementation

We have implemented the projection principle described in Sections 2.2.2 and 2.2.3 as follows:

- The *Epsilon* (ϵ) value (see Figure 4.5) is stored for filtering.
- We initialize the image to zero.
- For all the voxels of the volume to be reconstructed (which must be defined carefully, see Section 4.2.2) that are in the projection zone (defined by the six planes: sensor, emitter, top, bottom, right, left):
 1. We calculate their coordinates in the relative coordinate system and then the discrete column and row indices in the projected image (a 2D matrix).
 2. Once we have found the image pixel where the voxel will be projected, we add the voxel value to the pixel sum. This way, the “integral” shown in Equation 2.1 will be computed.
 3. Eventually, at least for tests, we can calculate here the partial projection matrix (only for one projection image) for the reconstruction part. The projection matrix is described in detail in Section 4.2.
 4. Next, we project on the same pixel all the voxels whose distance to the central one is smaller than ϵ . This is the *filtering* stage (described in Section 4.1.7).
 5. Finally, to obtain values to be displayed, we calculate the mean value of the densities projected on each pixel of the projection image.
- The resulting data are stored in files in order to be used in later processing. The final images are in bitmap (.bmp) format. Some examples of obtained images are in Figure 4.6.

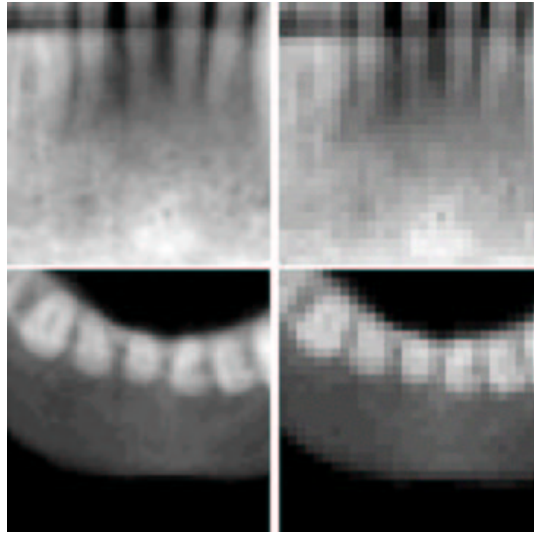


Figure 4.6: Some examples of projected images. On the left, two simulated radiographies with a pixel size of 0.5 mm. On the right side, the resolution is 1 mm/pixel.

4.1.7 Filtering

We can choose whether we want to add a *filter* to the projection process or not. This is characterized by the value of *Epsilon* (ϵ) in Figure 4.5. As we are working on a discrete geometry, this value defines the tolerance or, in our case, the distance (in mm) to the plane described by Equation 4.1. This means that, for example, a plane will have a “thickness” of 2ϵ mm for our processing. This filtering has to be done if we want to avoid the effect of discrete geometry. For instance, as we work with distances very close to the volume precision (voxel size), we could find that the number of voxels between two planes is very small or zero (because no voxel center has been found between the two planes). To be sure that any voxel “touched” by a pixel projection ray is taken into account to calculate the projection value, the ideal ϵ should be the half part of the largest distance between voxels, which is:

$$\epsilon_{ideal} = \frac{1}{2} \cdot \sqrt{PS^2 + PS^2 + ID^2}$$

In our case, we have $PS = 0.24$ mm (pixel size) and $ID = 0.5$ mm (interslice distance), what gives $\epsilon_{ideal} = 0.30$ mm. This will be the default value used if the *Epsilon* square is not activated. If it is, then when ϵ value is 0, there is no filtering (some black lines can appear in the projection image due to empty rays). When ϵ is different from zero, the introduced value in mm is used for processing.

Even if it is not the more appropriate terminology, we will call:

- *filtering* the process described above, as it contributes to lose precision in projected images, which means “filtering” high frequencies (this filtering processing is necessary to allow a visualization without *aliasing*);

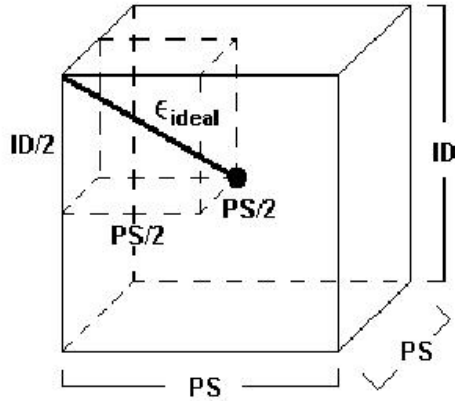


Figure 4.7: Geometrical explanation to find the ϵ_{ideal} for filtering. The cube represents a voxel.

- *aliasing* effect the resulting artifact on the projected images, if the ϵ value is not large enough (black lines or darker parallel zones).

4.2 Reconstruction implementation

As we have seen in Section 2.5, the reconstruction method we have chosen is SIRT. In this section the implementation of the SIRT method is described. But, first, there are two concepts that must be carefully detailed: the projection matrix and the reconstruction volume.

4.2.1 The projection matrix

The problem to be solved can be expressed in a matricial form (Chapter 2):

$$P = Rf \quad (4.2)$$

where

- P is the measure vector (in our case, the radiographic acquisitions) that has a size $m = M \times NP$ with M equal to the number of projections and NP equal to the number of pixels in a projection image (the same for all images);
- f is the vector that contains the searched values for each voxel of the volume to be reconstructed. This vector has a size n equal to the number of voxels in the volume;
- R is called projection matrix, with a size $m \times n$. This matrix only depends on the acquisition (not on the data) so its coefficients can be calculated once and for all. It is equivalent to the matrix \mathbf{X} of Equation 2.8.

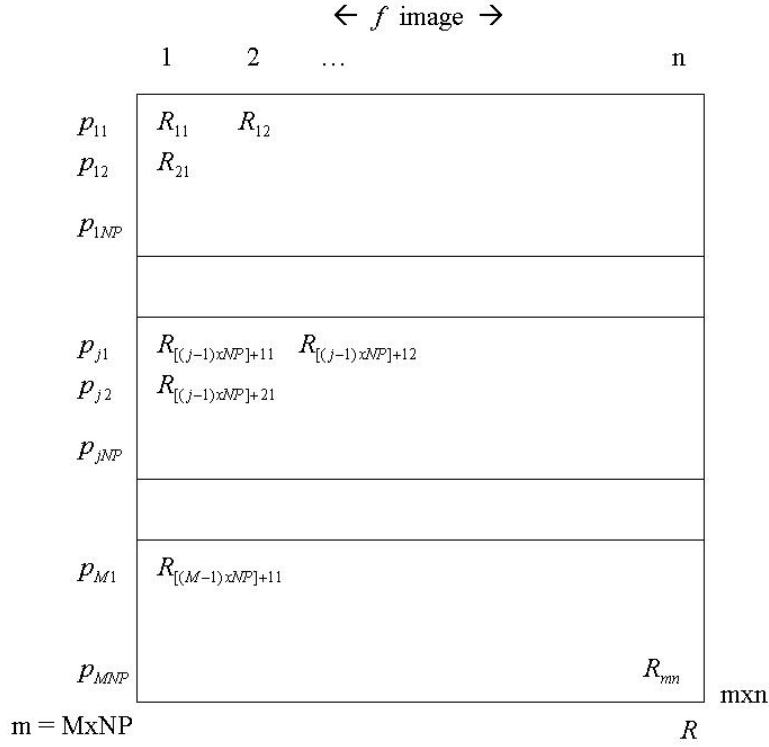


Figure 4.8: Projection matrix structure.

The structure of the projection matrix (shown in Figure 4.8) is the following:

- The matrix is made up of M submatrices. Each submatrix corresponds to one projection acquisition and it contains all the rays associated to its projection pixels. So the submatrix has NP lines (or rays) as NP is the number of pixels of the projection image (each pixel will have an associated ray).
- Each line in the matrix corresponds to a *ray*. We will call *ray* the vector of size n (the number of voxels in the volume: height \times width \times depth) that contains some *value* in the voxels touched by the pixel projection (the physical ray) and zero in the other voxels. The values that characterize the ray will be for the simplest case:

$$R_{ji} = \begin{cases} 1 & \text{if the ray } j \text{ touches voxel } i, \\ 0 & \text{otherwise.} \end{cases}$$

Figure 4.9 shows this principle in 2 dimensions to understand it more easily.

A more sophisticated version would consist in choosing the coefficients proportional to the volume of the intersection between the elementary volume of a voxel and the ray (which has a certain thickness):

$$R_{ji} \propto \text{overlapping volume between ray } j \text{ and voxel } i$$

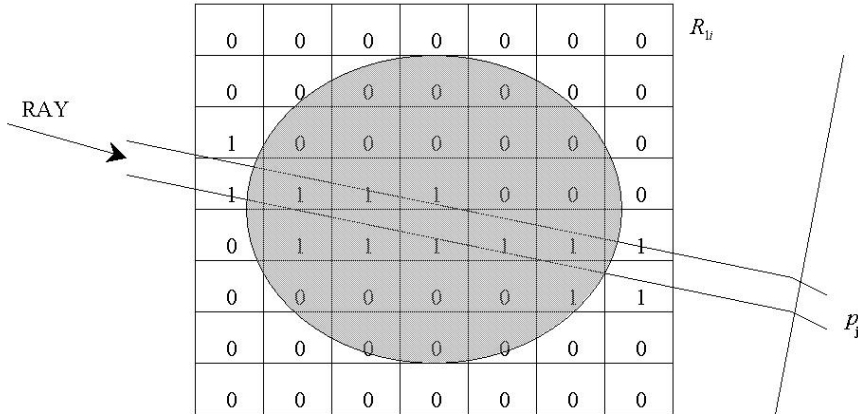


Figure 4.9: Matrix ray.

The first version only needs a bit to store each value, while the second one is more precise but it has higher memory costs.

Anyway, the projection matrix is usually a very big sparse matrix with a size of $(M \times NP) \times n$. Typically in our studies $n = 255 \times 255 \times 100$ (size of a CT scanner exam), $M = 8$ (maximal number of radiographic projections we can take) and $NP = 60 \times 60 = 3600$ (for example, with square projection images of $30 \text{ mm} \times 30 \text{ mm}$, and a resolution of 0.5 mm/pixel). If we store the value for every R_{ij} in a byte, then the projection matrix size will be about 200 GB, what shows one of the most important constraints for the implementation. This problem will lead us to try to store only *useful* values (different from zero). This will reduce the memory costs by a very important factor as the projection matrix is a sparse one. See implementation part for details (Appendix H).

Equation 4.2 translates the physical projection principle to a matricial operation. Thus, to see it more clearly, in the direct problem each point of the projection images (p_j) is obtained as the sum:

$$p_j = \sum_{i=1}^n R_{ji} f_i$$

where the ray associated to the point p_j ($R_{j\cdot}$) –a line of the matrix– is multiplied by the volume f –that is a vector too– so that an “integration” of the densities is done along this ray. See the equivalence with Equation 2.7.

This description is inspired in the 2D reconstruction methods detailed in [3].

4.2.2 The reconstruction volume

The volume to be reconstructed must be defined from the radiographic projections. This is not an easy problem and the reconstruction quality will depend on this volume definition.

The intersection of the parallelepipeds defined by the projections is the real volume to reconstruct or, better, this is the volume that can be “best” reconstructed because all the projections will add some information about it. However, as the shape of this volume could be very irregular, we would rather use a cube or a parallelepiped.

- If we take the largest parallelepiped inside the projection intersection, we could obtain a very small volume. However, the problem is that radiographies are the result of the X-ray projection through *all* the volume, not only through the reconstruction volume. Thus, voxels outside our reconstruction volume also contribute to the projection images. Therefore, when the inverse problem has to be solved, we will have the projections containing information coming from the voxels inside the volume we want to reconstruct but also from voxels outside this volume. It is not possible to know the contribution of voxels inside compared to voxels outside this volume. This means that we can not avoid having unnecessary information in our data. This problem will limit our reconstruction method and is one of the main points to study for further works.
- If we take the smallest parallelepiped including the projections intersection, there will be voxels that will not be optimally reconstructed (that is to say, not all the projections provide some information about these voxels because it is not inside their projection parallelepipeds). We use the second solution, but we must not forget its limits.

Therefore, the intersection of all projections is calculated and its bounding box defines the parallelepipedic volume to be reconstructed.

Another parameter that must be studied deeply is the size of the voxels to be reconstructed. This problem has been largely discussed and our conclusion is that it should be introduced in the interface by the user. Obviously, there is a strong link between the size of the voxels in the volume and the size of the pixels in the projections. It will be impossible to obtain a very good volume resolution from a poor projection resolution. In the best case, they will have the same order of magnitude.

4.3 Tests and measures

In this section we explain the different types of tests that have been made. The objective is to find the most appropriate regularization function (Tikhonov’s, Charbonnier’s or Huber’s) and then calculate the optimal parameters for the chosen function. Some preliminary results have been published in [24].

Error measure

The error used to measure the quality of our results is the Root Mean Square Error (RMSE). Equation 4.3 reminds us the principle of RMSE in a bidimensional case:

$$RMSE = \sqrt{\frac{\sum_{i,j}^{n,m} |x_{i,j} - y_{i,j}|^2}{n \times m}} \quad (4.3)$$

Test images

For our tests, we have used a three-dimensional phantom image (see Table 4.1), a real dry-jaw scanner image from an unknown person and a real (*in vivo*) scanner image (see Table 4.2).

Computing time

We will not speak about computing time of the implementation programs in this document. In the first version, the computing times were too high (some hours depending on the number of iterations and the resolution of the image). In the second version, realized by Manuel Deval, an important optimization stage was realized and computing times went down to 10 to 20 seconds for 2D images. Unfortunately, the three-dimensional version of the whole program could not be finished and computing times for these cases were not measured.

4.3.1 Influence of the number of projections

One of the main parameters that modify the quality of the result is the number of projection used for reconstruction. It is easy to understand that the larger the number of projections, the lower the error of the resulting volume. This is illustrated in Fig. 4.10.

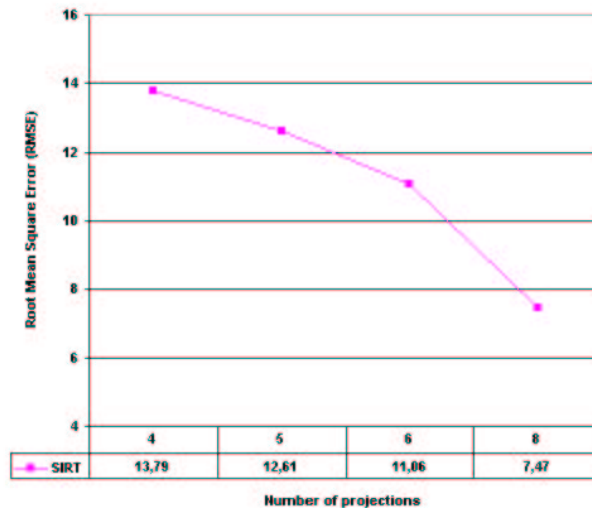


Figure 4.10: RMSE comparison for reconstruction with a different number of projections.

The effect of the number of projections on the resulting quality can be observed in Fig. 4.11 too, where several RMSE values with different λ and α (from Huber's function) are compared in the case of using 4 projections or 8 projections for the reconstruction.

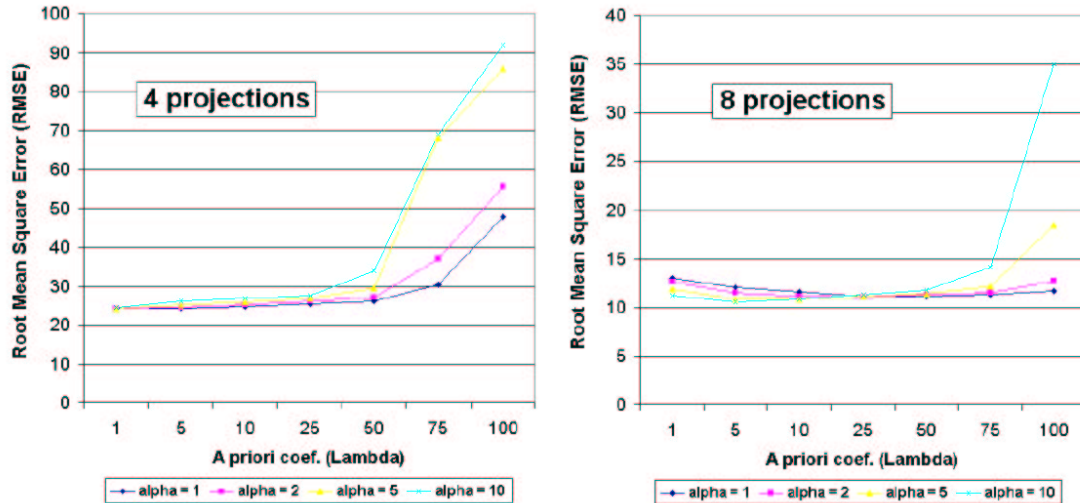


Figure 4.11: RMSE comparison for several λ and α (from Huber's function) combinations when 4 projections (left) and 8 projections (right) are used for the reconstruction.

The images in Table 4.2 also show the quality of the results with 4 and 8 projections.

Conclusion

As it is obvious that the quality of the reconstruction is better with a large number of projection, we will use the maximal number of projections we are allowed to: 8 projections.

4.3.2 Influence of the regularization functions

Figures 4.12 and 4.13 show the different results obtained with the regularization functions that have been implemented. As explained in Chapter 3, the most appropriate regularization functions are Charbonnier's and Huber's ones. Here we compare the results obtained with both of them and the classical regularization function of Tikhonov.

Table 4.1 shows visually the different quality of the results for the phantom image in the case of using only the SIRT method, the SIRT method plus Charbonnier's regularization and the SIRT method plus Huber's regularization. The parameters used for the regularization stage must be chosen between certain limits; otherwise, some "curious" results may be obtained (see Table I.1 in Appendix I).

Conclusion

If we observe the previous images, we conclude that the quality increases if a regularization method is added to the reconstruction with an algebraic method. Charbonnier

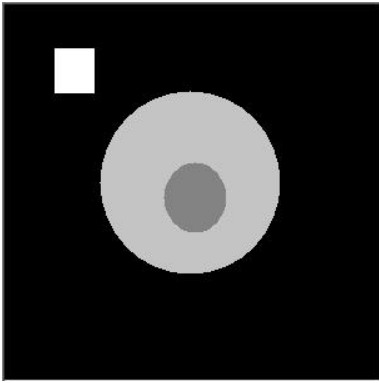
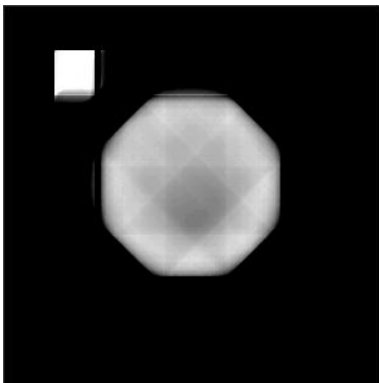
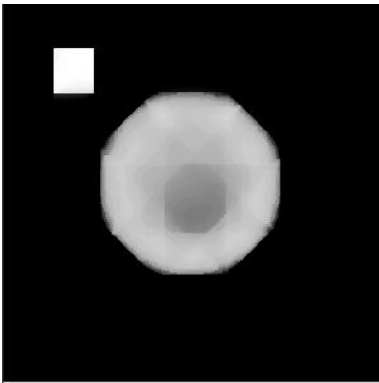
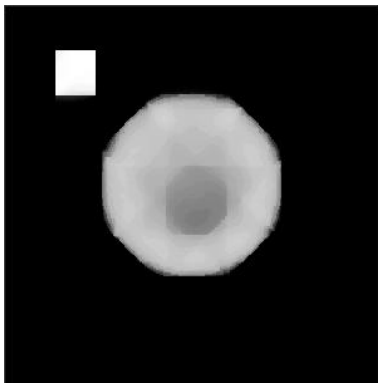
		
Original phantom image		
		
Image reconstructed with SIRT	Image reconstructed with SIRT and regularized with Charbonnier's method $\lambda = 95$	Image reconstructed with SIRT and regularized with Huber's method $\alpha = 2$ $\lambda = 50$

Table 4.1: Comparative table of a resulting reconstructed cut of the phantom for 1000 iterations.

or Huber regularization should furnish better results than the classical Tikhonov regularization. Previous graphics show that this is not always true. Our conclusion is that Tikhonov regularization can be appropriate for some values of the *a priori* parameter λ for some particular images. However, results depend too much on the number of projections and on the value of λ . So, for images such as those from our case, and as explained in Chapter 3, Charbonnier's or Huber's regularizations are a better option than Tikhonov's one.

4.3.3 The optimal parameters of the regularization function

Both Charbonnier and Huber functions allow to obtain equivalent results in terms of our quality criterion (RMSE). However, the advantage of Huber’s function is that it furnishes one more parameter (α) to “play with”. This is why, we continued our optimization stage with this function.

Table 4.2 shows some results obtained with different reconstruction algorithms without (ART and SIRT) and with (SIRT with Huber’s function) regularization.

Figures 4.14 to 4.19 illustrate the different tests performed in order to find the optimal parameters α and λ for which the best results are obtained.

Conclusion

Table 4.2 shows clearly that the results are much better with 8 projections than with only 4. The regularization effects are easily appreciated in the dry jaw images with 4 projections as some homogeneous regions appear and the hole of the dental canal and the cortical bone are better distinguished for an appropriate choice of the parameters. Nevertheless, with 8 projections the difference with no regularized images is very little. The reconstructed images for the dry jaw are very satisfying but for a real *in vivo* case some processing must be added or modified because the influence of the intensity values of the skin and other matters worsen the quality of the results.

Figures 4.14 to 4.19 show the resulting RMSE for different combinations of parameters λ and α (from Huber’s regularization function). The influence of the regularization parameters is as follows:

- when λ is higher, more noise is filtered,
- when α (see Huber equation in Table 3.1) increases, then larger differences between neighbors are smoothed (as it is described in Chapter 3 and in [34]).

So, we have to look for the best parameter combination (α and λ) in each case. For each image, the optimal combination of parameters will be different and, as it can be seen in the previous graphics, this combination varies also depending on whether reconstruction is made from 4 or 8 projections. Next table shows the optimal parameter combinations for the test performed using the regularization function of Huber and a number of iterations equal to 100:

	4 projections		8 projections	
	λ	α	λ	α
Phantom image	75	2	100	10
Dry jaw	1	2	5	10
<i>In vivo</i> application	50	5	100	10

It can be observed on the graphics that the results obtained for the *in vivo* image have some irregular behavior. As we said before, this is the case of a real *in vivo* image and it will require some additional processing to obtain satisfying results. So, the optimal parameters for this particular case are not very representative.

4.4 Conclusion

We have found several pairs of optimal parameters for some particular cases. However, the same combination is not the optimal one for different images. This is a problem because the characteristics of the image to be reconstructed are not known in advance and so, how could the most appropriate parameters be chosen?

The answer is not easy. The same pair of parameters should only be used for similar images: same contrast levels, similar homogeneity properties, same quality (noise), same number of projections... Some of these characteristics vary from one patient to another. Some of them vary within the same patient depending on the zone to be reconstructed. This means that the optimal combination depends on the patient and the projection geometry which calls for further investigation.

An idea could be to “estimate” the kind of image to be obtained and use the most appropriate “optimal parameters” for this kind of image. Obviously, a data base of images and their associated optimal parameters should be done before.

Future work aims at adding other *a priori* information obtained from statistical models of the mandibular bone densities, so that it will be easier to find visually in the reconstructed images the dental canal and the cortical bone of the jaw.

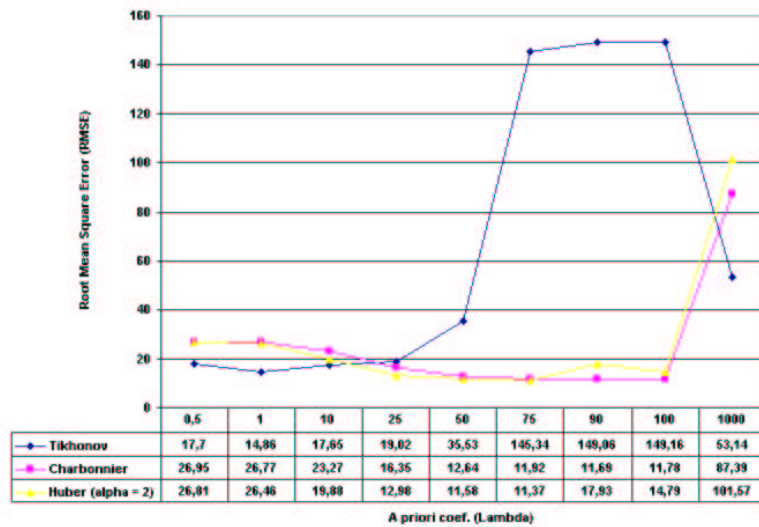


Figure 4.12: RMSE comparison for different regularization functions on the phantom image. Number of iterations = 100; Number of projections = 4.

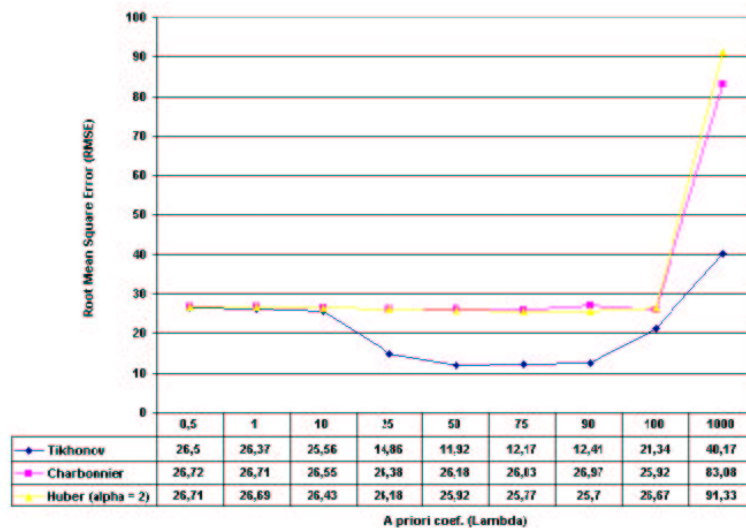


Figure 4.13: RMSE comparison for different regularization functions on the phantom image. Number of iterations = 100; Number of projections = 8.



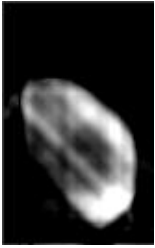
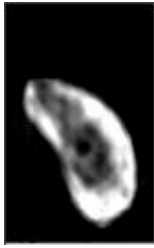
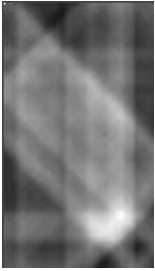
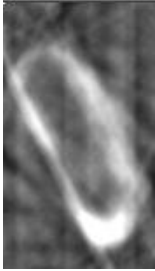



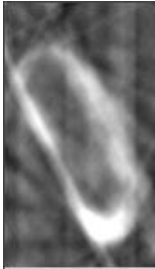
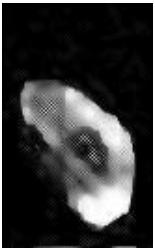







	Dry jaw		<i>In vivo</i> application	
Original				
	4 projections	8 projections	4 projections	8 projections
ART				
SIRT				
Regularized SIRT $\alpha = 5$ $\lambda = 50$				
Regularized SIRT $\alpha = 2$ $\lambda = 5$				

Table 4.2: Comparative table of resulting reconstructed cuts of the jaw for 100 iterations.

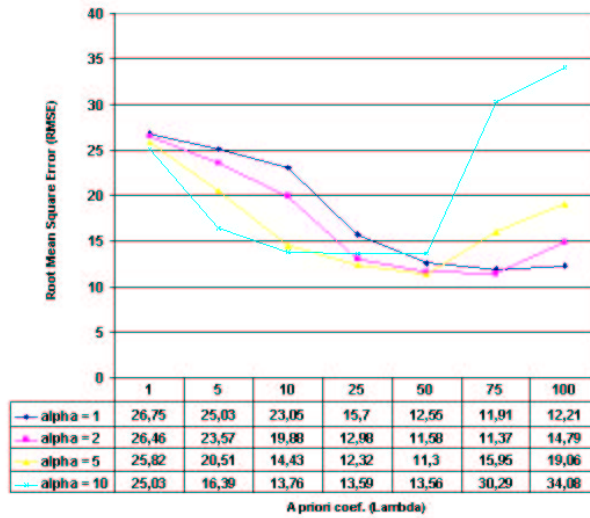


Figure 4.14: RMSE comparison for different combinations of λ and α with 4 projections on a phantom image. The potential function used is Huber's one and the number of iterations is 100.

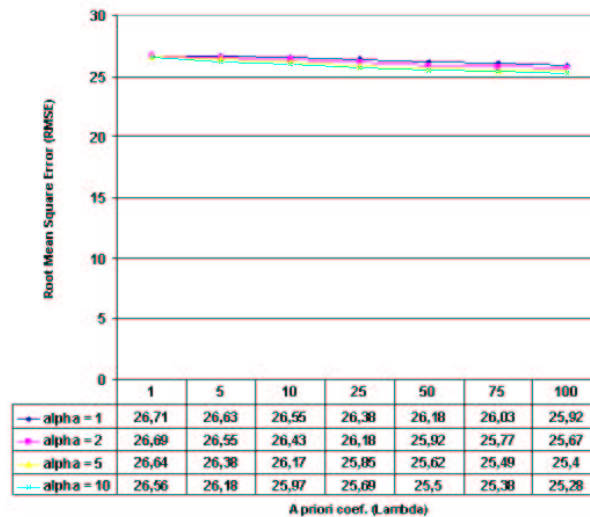


Figure 4.15: RMSE comparison for different combinations of λ and α with 8 projections on a phantom image. The potential function used is Huber's one and the number of iterations is 100.

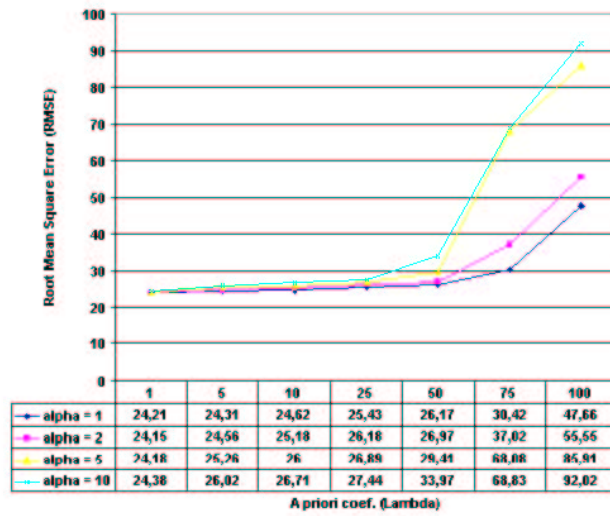


Figure 4.16: RMSE comparison for different combinations of λ and α with 4 projections on a dry jaw. The potential function used is Huber's one and the number of iterations is 100.

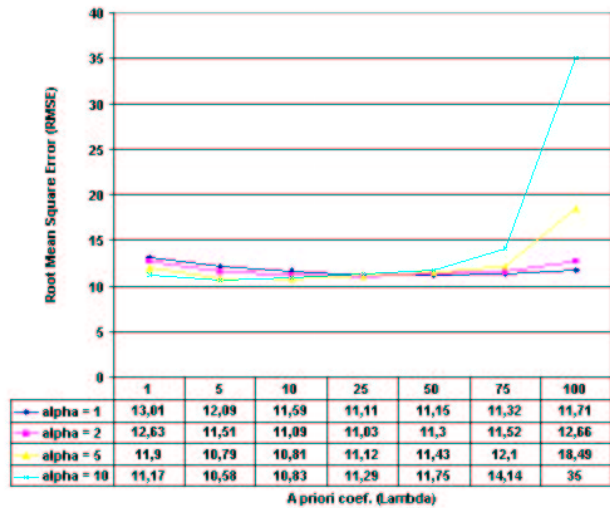


Figure 4.17: RMSE comparison for different combinations of λ and α with 8 projections on a dry jaw. The potential function used is Huber's one and the number of iterations is 100.

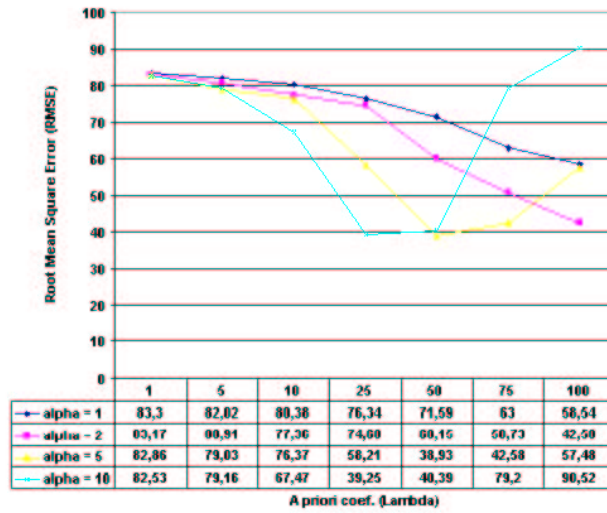


Figure 4.18: RMSE comparison for different combinations of λ and α with 4 projections for an *in vivo* application. The potential function used is Huber's one and the number of iterations is 100.



Figure 4.19: RMSE comparison for different combinations of λ and α with 8 projections for an *in vivo* application. The potential function used is Huber's one and the number of iterations is 100.

Chapter 5

Conclusion and future work

Conclusions

In Chapter 2 we have concluded that the possibility of adding *a priori* information and the adaptability to different geometries are the necessary criteria for our reconstruction problem (introduced in Chapter 1). This is difficult to incorporate in analytical methods. So, despite their good behavior in terms of computing time and the fact that they are already largely used for similar applications, we have not chosen them to develop our work. Although statistical methods are more stable and more robust against noise than the other kinds of methods, they are often very complex to implement for a resulting quality not as good as it could be expected. And structural methods are mainly useful for binary reconstructions so they are not adapted to our specific case.

Therefore, we have chosen algebraic methods ART and SIRT because they allow us to easily introduce *a priori* information without having a very heavy implementation and they are adaptable to different geometries. The disadvantages of this kind of methods are that their computing times and memory costs are a little high and that they are not very robust against noise. This will lead us to introduce regularization constraints.

In Chapter 3 the *semi-quadratic minimization* algorithm has been chosen for our implementation because this method provides convergence towards a global minimum in the case of a potential function ϕ which is not convex and with the constraint of a sparse projection matrix. Moreover, this algorithm does not depend on the initialization, which is very convenient for a medical application. In addition to the convergence advantages, this algorithm is also interesting from a point of view of the computer implementation.

Finally in Chapter 4 we have found several pairs of optimal parameters of the algorithm for some particular cases. However, the same combination is not the optimal one for different images. The same pair of parameters should only be used for similar images: same contrast levels, similar homogeneity properties, same quality (noise), same number of projections... Some of these characteristics vary from one patient to another. Some of them vary within the same patient depending on the zone to be reconstructed.

Future work

Future works will have to improve and optimize some of the choices we made and there are new ways to be explored.

For example, the error measure we have used is the Root Mean Square Error (RMSE). This choice may be discussed, other error measures could be better adapted.

The projection matrix can also be improved. A more sophisticated version would consist in choosing the coefficients proportional to the volume of the intersection between the elementary volume of a voxel and the ray (which has a certain thickness):

$$R_{ji} \propto \text{overlapping volume between ray } j \text{ and voxel } i$$

One of the main problems to discuss is the definition of the reconstruction volume. As we described in Section 4.2.2 the choice of the volume to reconstruct is not easy and the limits of our choice call for further investigation.

In Chapter 4 we have shown that the reconstructed images for the dry jaw are very satisfying but for a real *in vivo* case some processing must be added or modified because the influence of the intensity values of the skin and other matters worsen the quality of the results.

As we have said above, the optimal parameter combination for our algorithm depends on the patient and the projection geometry and further investigation is necessary. An idea could be to “estimate” the kind of image to be obtained and use the most appropriate “optimal parameters” for this kind of image. This implies the previous creation of a data base of images and their associated optimal parameters.

Other solution to this problem, which would be an innovation, is to add other *a priori* information obtained from statistical models of the mandibular bone densities, so that it will be easier to find visually in the reconstructed images the dental canal and the cortical bone of the jaw.

Appendix A

Introduction to the Radon transform

A.1 Definition

In a general way, the Radon transform associates to a function of n variables its integrals on the hyper-planes of \mathfrak{R}^n . It is the mathematical operator that expresses the observed projections of a function f of \mathfrak{R}^n .

$$R f(u, \theta) = p_\theta(u) = \int_{-\infty}^{+\infty} \int_{-\infty}^{+\infty} f(x, y) \delta(x \cos \theta + y \sin \theta - u) dx dy \quad (\text{A.1})$$

For instance, for the case of $n = 2$, the Radon transform represents the integral of a function on the right lines of a plane (see Equation A.1), and in the case of $n = 3$, it represents the integral on the planes of the space. It can be expressed with the Dirac distribution on \mathfrak{R}^n (written as δ).

The most interesting property with respect to our application is the inversibility of this transformation, that is to say, the possibility of determining f from $R f$.

For more information about the Radon transform see [17], [3], [29].

A.2 Inversion formulas [29]

The problem of the inversion of the Radon transform has been solved in the general case (for any n). There are some analytical inversion formulas which allow to express f in function of $R f$ for n even or odd. Here we just recall these relations without proof. The inversion of the Radon transform utilizes the associated operator of this transformation, known in tomography as the *backprojection operator*. It is written for any function h , defined on $\mathfrak{R} \times S^{n-1}$ (where S^{n-1} is the unitary sphere of \mathfrak{R}^n) as:

$$B f(x) = \int_{S^{n-1}} h(x \cdot \theta, \theta) d\theta \quad (\text{A.2})$$

So, the inversion formulas are formally expressed in the following way:

- if n is even:

$$f = \frac{1}{2(2i\pi)^{n-2}} B H D_r^{n-1} R f \quad (\text{A.3})$$

- if n is odd:

$$f = \frac{1}{2(2i\pi)^{n-1}} B H D_r^{n-1} R f \quad (\text{A.4})$$

where H indicates the Hilbert transformation on \mathfrak{R} , and D_r the partial differentiation operator according to the variable r .

In tomography, these formulas are seldom used like this, but they provide a formal framework to the problem of reconstruction from projections.

Appendix B

Projection theorem

The projection theorem allows to understand that all the information about the image is contained in the set of projections. It says that the mono-dimensional Fourier transform of the projection of a function $f(x, y)$ is a cut of the bidimensional Fourier transform of the function. That is to say:

$$F_1 p_\theta(U) = F_2 f(U \cos \theta, U \sin \theta) \quad (\text{B.1})$$

where F_1 represents the mono-dimensional Fourier transform and F_2 the bidimensional Fourier transform.

So, when θ varies between 0 and π , we have access to the totality of the Fourier transform of the image in polar coordinates, and so, we can find the image itself. In the same way, we can see that if the acquisition is done on an angular sector strictly lower than π , there will be some missing data in the “Fourier plane”. Then, the image is not determined anymore in an exact way from the acquisition, and the problem will become severely ill-posed.

Appendix C

3D backprojection operator

The divergent 3D backprojection operator, noted B , associates to the set of conical projections p_τ , when the direction τ varies, a three-dimensional image defined by:

$$B p(\mathbf{r}) = \int_{\Omega} p_\tau(\mathbf{r}_\tau) d\omega_\tau \quad (\text{C.1})$$

where ω_τ is the variable of the angular integration and Ω is the domain of the angular integration (both are defined by the trajectory), and where \mathbf{r}_τ is the projection of vector \mathbf{r} on the plane π_τ (see Figure C.1):

$$\mathbf{r}_\tau = D \left(\frac{\mathbf{r} - (\mathbf{r} \cdot \boldsymbol{\tau}) \boldsymbol{\tau}}{D_1 - \mathbf{r} \cdot \boldsymbol{\tau}} \right) \quad (\text{C.2})$$

$$\text{with } D = D_1 + D_2$$

where D is the distance between S and S' , D_1 is the distance between S and O , and D_2 is the distance between O and S' in Figure C.1.

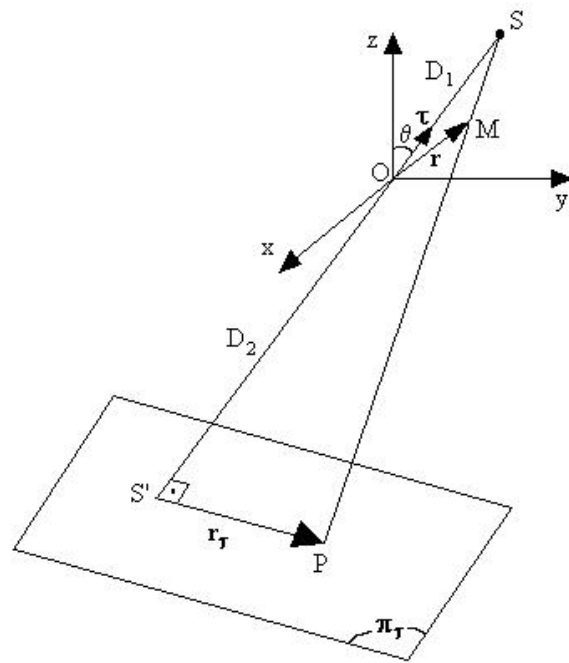


Figure C.1: Projection of a vector r on a plane π_τ .

Appendix D

Bayesian estimation

The Bayesian approaches allow to express the *a posteriori* distribution $P(\mathbf{x}|\mathbf{y})$ as a function of:

- the likelihood of the data compared to the original object $P(\mathbf{y}|\mathbf{x})$,
- the *a priori* which is the distribution of the probability $P(\mathbf{x})$,
- $P(\mathbf{y})$ as a normalization constant.

The Bayes formula (already shown in Equation 2.17) is:

$$P(\mathbf{x}|\mathbf{y}) = \frac{P(\mathbf{y}|\mathbf{x}) P(\mathbf{x})}{P(\mathbf{y})}$$

In order to obtain the estimate of the object $\hat{\mathbf{x}}$ from the distribution $P(\mathbf{x}|\mathbf{y})$, a Bayesian estimator is used. There are several different methods, among which the three main estimators are:

- The Maximum A Posteriori (MAP) estimator:

$$\hat{\mathbf{x}}_{MAP} = \text{Argmax}_{\mathbf{x}} P(\mathbf{x}|\mathbf{y}) \quad (\text{D.1})$$

- The *a posteriori* mean (MP) estimator:

$$\hat{\mathbf{x}}_{MP} = \int \mathbf{x} P(\mathbf{x}|\mathbf{y}) d\mathbf{x} \quad (\text{D.2})$$

- The *a posteriori* Marginal Modes (MMP) estimator:

$$\hat{\mathbf{x}}_{MMP} = \text{Argmax}_{\mathbf{x}_s \in \omega} P(\mathbf{x}_s|\mathbf{y}) \quad (\text{D.3})$$

The Maximum A Posteriori (MAP) estimator is the most classical method because it can be implemented most of the time. It is often used in most of image analysis problems such as noisy images restoration and image segmentation. This method allows to do the link with the deterministic approaches used in regularization. Better than maximizing the *a posteriori* distribution, it is preferred in general to minimize this quantity:

$$-\log [P(\mathbf{x}|\mathbf{y})] \sim - \underbrace{\log [P(\mathbf{y}|\mathbf{x})]}_{\text{Attach to the data}} - \underbrace{\log [P(\mathbf{x})]}_{a \text{ priori}} \quad (\text{D.4})$$

This is called minimization of the *log-likelihood* of the object knowing the data. So, from this equation of the estimator, it is very easy to separate the data from the *a priori*.

See, for instance, [21] and [2] for details.

Appendix E

Maximum of Entropy Principle

The Maximum of Entropy principle can be summarized as follows:

Let x be a continuous variable and we suppose that an information $E\{\Phi_k(x)\} = d_k$ (where $k = 1, \dots, K$) has to be translated by a probability law $p(x)$. Which law $p(x)$ must be chosen among the infinity of laws that fulfill the constraints?

The answer furnished by the maximum of entropy principle is to choose the law $p(x)$ that has the maximal entropy S :

$$S = - \int p(x) \log p(x) dx$$

The solution is written this way:

$$p(x) = \frac{1}{Z} \exp \left(- \sum_{k=1}^K \lambda_k \phi_k(x) \right)$$

where $\{\lambda_k, k = 1, \dots, K\}$ are the Lagrange multipliers which are calculated from $\{d_k, k = 1, \dots, K\}$ (see [29]).

Appendix F

Minimization algorithm of Delaney and Bresler [8]

Let $J_0(\mathbf{f}, e)$ be:

$$J_0(\mathbf{f}, e) = Q(\mathbf{f}) + \lambda^2 \sum_{m=0}^{M-1} e_m V_m(\mathbf{f}) \quad (\text{F.1})$$

This function is strictly convex because of the properties of Q and V_m . The algorithm follows an iterative scheme of this form:

$$\mathbf{f}^{k+1} = \mathcal{M}(\mathbf{f}^k) \quad (\text{F.2})$$

with

$$\mathcal{M}(\mathbf{f}^k) = \arg \min_w \left\{ J_0[w, \Phi[V_m(\mathbf{f}^k)]] \right\} \quad (\text{F.3})$$

The minimization of the function in F.3 does not have any particular problem for J_0 is convex compared to w . At each iteration k , first, the minimum of $J_0[w, \Phi[V_m(\mathbf{f}^k)]]$ is searched (helped, for example, by a gradient descent method); this minimum furnishes the value of \mathbf{f}^{k+1} that gives the new function $J_0[w, \Phi[V_m(\mathbf{f}^{k+1})]]$, and so on. The convergence of this algorithm has been proved [8] in the case of a non-convex potential function ϕ with the constraint of a sparse matrix \mathbf{X} too.

Appendix G

Implementation of the semi-quadratic minimization algorithm

The process of reconstruction/regularization is based on a double loop. First, the auxiliary variable b is calculated. Then, a gradient descent algorithm is used to minimize the function in Equation 3.14 with respect to \mathbf{f} (other algorithms may be used too). When this minimization is done, the auxiliary variables are calculated again with the last update of \mathbf{f} and the process is restarted. These stages are successively repeated until a stop criterion.

The following schema shows the used implementation of the algorithm ARTUR:

Repeat

1. Calculate the auxiliary variables

$(b_x^{k+1})_{i+1,j,k} = \frac{\phi'[\mathbf{f}_{i+1,j,k}^k - \mathbf{f}_{i,j,k}^k]}{2[\mathbf{f}_{i+1,j,k}^k - \mathbf{f}_{i,j,k}^k]}$	$(b_x^{k+1})_{i-1,j,k} = \frac{\phi'[\mathbf{f}_{i,j,k}^k - \mathbf{f}_{i-1,j,k}^k]}{2[\mathbf{f}_{i,j,k}^k - \mathbf{f}_{i-1,j,k}^k]}$
$(b_y^{k+1})_{i,j+1,k} = \frac{\phi'[\mathbf{f}_{i,j+1,k}^k - \mathbf{f}_{i,j,k}^k]}{2[\mathbf{f}_{i,j+1,k}^k - \mathbf{f}_{i,j,k}^k]}$	$(b_y^{k+1})_{i,j-1,k} = \frac{\phi'[\mathbf{f}_{i,j,k}^k - \mathbf{f}_{i,j-1,k}^k]}{2[\mathbf{f}_{i,j,k}^k - \mathbf{f}_{i,j-1,k}^k]}$
$(b_z^{k+1})_{i,j,k+1} = \frac{\phi'[\mathbf{f}_{i,j,k+1}^k - \mathbf{f}_{i,j,k}^k]}{2[\mathbf{f}_{i,j,k+1}^k - \mathbf{f}_{i,j,k}^k]}$	$(b_z^{k+1})_{i,j,k-1} = \frac{\phi'[\mathbf{f}_{i,j,k}^k - \mathbf{f}_{i,j,k-1}^k]}{2[\mathbf{f}_{i,j,k}^k - \mathbf{f}_{i,j,k-1}^k]}$

2. Minimization with fixed b : modified gradient descent

$$\mathbf{f}^{k+1,0} = \mathbf{f}^k$$

Repeat

For (i, j, k) from 1 to N :

- Calculate

$$\begin{aligned}
L_{i,j,k} = & (\mathbf{f}_{i+1,j,k}^{k+1,l} - \mathbf{f}_{i,j,k}^{k+1,l}) \cdot (b_x^{k+1})_{i+1,j,k} + (\mathbf{f}_{i,j,k}^{k+1,l} - \mathbf{f}_{i-1,j,k}^{k+1,l}) \cdot (b_x^{k+1})_{i-1,j,k} + \\
& + (\mathbf{f}_{i,j+1,k}^{k+1,l} - \mathbf{f}_{i,j,k}^{k+1,l}) \cdot (b_y^{k+1})_{i,j+1,k} + (\mathbf{f}_{i,j,k}^{k+1,l} - \mathbf{f}_{i,j-1,k}^{k+1,l}) \cdot (b_y^{k+1})_{i,j-1,k} + \\
& + (\mathbf{f}_{i,j,k+1}^{k+1,l} - \mathbf{f}_{i,j,k}^{k+1,l}) \cdot (b_z^{k+1})_{i,j,k+1} + (\mathbf{f}_{i,j,k}^{k+1,l} - \mathbf{f}_{i,j,k-1}^{k+1,l}) \cdot (b_z^{k+1})_{i,j,k-1}
\end{aligned}$$

- Update:

$$\mathbf{f}_{i,j,k}^{k+1,l+1} = \underbrace{\mathbf{f}_{i,j,k}^{k+1,l} + \delta t [\mathbf{X}^T(\mathbf{p} - \mathbf{X}\mathbf{f})]}_{\text{Type ART update}} - \underbrace{\delta t \lambda^2 L_{i,j,k}}_{\text{Regularization}}$$

Until convergence

$$\mathbf{f}^{k+1} = \mathbf{f}^{k+1,l+1}$$

Until convergence

Compared to ART, the regularization term $\delta t \lambda^2 L_{i,j,k}$ is added into the function to minimize. In the update formula, we find the parameter λ which weighs the fidelity to the data compared to the *a priori*, and the parameter δt which is the relaxation factor analog to the one used in ART (Section 2.4.3).

Appendix H

The reconstruction implementation

A C++ class-based implementation has been used to develop the different algorithms we have used. The main class is “Reconstruction Technique”.

Class ‘Reconstruction Technique’

This is the main class. It is defined as a list of lists where each node of the main list represents a projection pixel and the list starting in this node represents the ray that is projected on this pixel. The nodes in the main list contain the intensity value of the pixel, a pointer to a list (ray) and the number of cells in this ray. The partial list (ray) contains some cells corresponding to the voxels that are “touched” by this ray. These cells store the voxel coordinates and the weight of this voxel for this ray (1 in the first version¹).

The preprocessing functions defined in this class are:

- `randomize_projections_order`: randomize the order of the projections before the processing. It has been proved that results are better because the differences between projections is larger. There are less differences between physically next projections.
- `suppress_null_projection_voxels`: only the voxels whose the projection is not null are stored and processed. This is done to optimize computing time and memory costs (in the first versions all voxels were treated).

Class ‘art’

This class inherits from ‘Reconstruction Technique’. The functions defined here are:

- `compute_one_iteration`: this is the real implementation of the algorithm.
- `get_relax_coef`: gets the relaxation coefficient (λ).

The steps of `compute_one_iteration` are:

- $R_j * f$

¹Voxels with *value* = 0 are not stored.

- $\lambda * (p_j - R_j * f) / ||R_j||^2 \rightarrow f^{k+1}$
- Update:
 - positivity: $\begin{cases} \text{if voxel value} < 0 \Rightarrow 0 \\ \text{if voxel value} > 255 \Rightarrow 255 \text{ (8 bits values)} \end{cases}$

Class ‘sirt’

This class inherits from class ‘art’.

The steps of `compute_one_iteration` are:

- $P - R * F$
- $Rt * (P - R * F)$
- Update:
 - $\lambda * Rt * (P - R * F)$
 - positivity: $\begin{cases} \text{if voxel value} < 0 \Rightarrow 0 \\ \text{if voxel value} > 255 \Rightarrow 255 \text{ (8 bits values)} \end{cases}$

Class ‘SirtArt’

This class inherits from class ‘Reconstruction Technique’. It performs one iteration ‘art’ and then one iteration ‘sirt’, one iteration ‘art’ and then one iteration ‘sirt’, etc.

Class ‘SirtReg’

This class inherits from class ‘sirt’. The functions defined here are:

- `compute_one_iteration`.
- `Huber_pot_function`: computes the Huber function.
- `Huber_deriv_pot_function`: computes the derived Huber function.
- `get_a_priori_coef`: gets the *a priori* coefficient ($\lambda_{equation}$).

The steps of `compute_one_iteration` are:

- Calculation of bx , by , bz and the differences for L_{ijk} (see Appendix G)
- $P - R * F$
- $Rt * (P - R * F)$
- L_{ijk}
- Update:
 - $\lambda * (Rt * (P - R * F)) = error_{ART}$ (equivalent to ART error)

- $\lambda * \lambda_{equation} * L_{ijk} = ErrorReg$ (regularization term)
- $F^{k+1} = F^k + errorART - ErrorReg$
- positivity: $\begin{cases} \text{if voxel value} < 0 \Rightarrow 0 \\ \text{if voxel value} > 255 \Rightarrow 255 \text{ (8 bits values)} \end{cases}$

Appendix I

Strange effects of wrong regularization

The parameters used for the regularization stage must be chosen between certain limits; otherwise, some strange results may be obtained as shown in Table I.1.

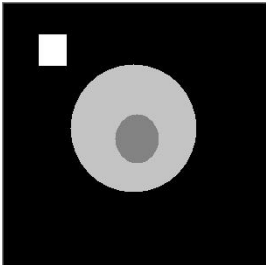
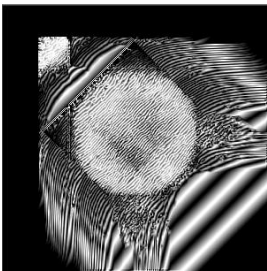
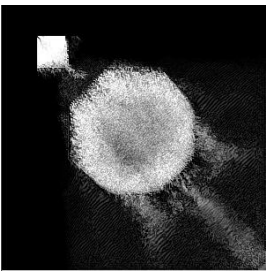
	
Original phantom image	
	
<i>Fish effect</i> Image reconstructed with SIRT and regularized with Charbonnier's method <i>130 iterations</i> $\lambda = 1000$	<i>Comet effect</i> Image reconstructed with SIRT and regularized with Charbonnier's method <i>1000 iterations</i> $\lambda = 100$

Table I.1: Some strange effects of regularization that we have obtained with an inappropriate choice of the parameters for a cut of the phantom.

Bibliography

- [1] G. Aubert, M. Barlaud, L. Blanc-Féraud, and P. Charbonnier. A deterministic algorithm for edge-preserving computed imaging using Legendre transform. In *12th International Conference on Pattern Recognition (ICPR)*, volume 3, pages 188–191, Jerusalem, Israel, October 1994.
- [2] P. Bleuet. *Reconstruction 3D par tomosynthèse généralisée. Application à l'imagerie médicale par rayons X*. PhD thesis, 02ISAL0059, Institut National des Sciences Appliquées (INSA), Lyon, October 2002.
- [3] I. Bloch. Reconstruction d'images tomographiques. Cours du module SIM (Systèmes d'Imagerie Médicale), École Nationale Supérieure des Télécommunications, département TSI, 2000.
- [4] O. Cámara. Reconstruction cardiaque 4D. Déformation dans des volumes cardiaques. Technical report, Département des Applications Avancées, General Electric Medical Systems Europe and département TSI, Ecole Nationale Supérieure des Télécommunications, Paris, apr-nov 2000. Rapport bibliographique du mastère IST.
- [5] P. Charbonnier. *Reconstruction d'image : régularisation avec prise en compte des discontinuités*. PhD thesis, Université de Nice - Sophia Antipolis, September 1994.
- [6] P. Charbonnier, G. Aubert, L. Blanc-Féraud, and M. Barlaud. Two deterministic half-quadratic regularization algorithms for computed imaging. In *IEEE International Conference on Image Processing (ICIP)*, volume 2, pages 168–172, Austin, USA, November 1994.
- [7] P. Charbonnier, L. Blanc-Féraud, G. Aubert, and M. Barlaud. Deterministic edge-preserving regularization in computed imaging. *IEEE Transactions on Image Processing*, 6(2):298–311, February 1997.
- [8] A.H. Delaney and Y. Bresler. Globally convergent edge-preserving regularized reconstruction: An application to limited-angle tomography. *IEEE Transactions on Image Processing*, 7(2):204–221, 1998.
- [9] R.V. Denton, B. Friedlander, and A.J. Rockmore. Direct three-dimensional image reconstruction from divergent rays. *IEEE Transactions on Nuclear Science*, NS-26(5):4695–4703, 1979.
- [10] J.M. Dinten. *Tomographie à partir d'un nombre limité de projections, régularisation par des champs markoviens*. PhD thesis, Université Paris XI, 1990.

- [11] P.P.B. Eggermont, G.T. Herman, and A. Lent. Iterative algorithms for large partitioned linear systems with applications to image reconstruction. *Linear algebra and its applications*, 40:37–67, 1981.
- [12] L.A. Feldkamp, L.C. Davis, and J.W. Kress. Practical cone-beam algorithm. *Journal of the Optical Society of America A*, 1(6):612–619, June 1984.
- [13] L. Garnero. *Reconstruction d'images tomographiques à partir d'un ensemble limité de projections*. PhD thesis, Université Paris-Sud, 1987.
- [14] D. Geman and G. Reynolds. Constrained restoration and the recovery of discontinuities. *IEEE Transactions on Pattern Recognition and Machine Intelligence*, 14(3):367–383, 1992.
- [15] R. Gordon, R. Bender, and G.T. Herman. Algebraic reconstruction technique (ART) for three-dimensional electron microscopy and X-ray photography. *Journal of Theoretical Biology*, 29:471–481, 1970.
- [16] P. Grangeat. *Analyse d'un système d'imagerie 3D par reconstruction à partir de radiographies X en géométrie conique*. PhD thesis, École Nationale Supérieure des Télécommunications, Paris, 1987.
- [17] S. Hammer. Reconstruction 3D à partir d'un nombre limité de projections en imagerie médicale. Technical report, Département TSI, Ecole Nationale Supérieure des Télécommunications, Paris, mar 2002.
- [18] G.M. Hounsfield. A method of an apparatus for examination of a body by radiation such as X-ray or gamma radiation. Patent Specification number 1283915, The Patent Office, 1972.
- [19] P. J. Huber. *Robust Statistics*. John Wiley & Sons, New York, 1981.
- [20] A.C. Kak and M. Slaney. *Algebraic Reconstruction Algorithms*, chapter 7. IEEE Press, 1998.
- [21] C. Klifa. *Reconstruction tridimensionnelle d'objets à partir d'un nombre très limité de projections. Applications à la radiographie industrielle*. PhD thesis, TELECOM Paris 91E008, École Nationale Supérieure des Télécommunications, Paris, May 1991.
- [22] H. R. Künsch. Robust priors for smoothing and image restoration. In *Annals of the Institute of Statistical Mathematics*, volume 46, pages 1–19, 1994.
- [23] A.K. Louis and P. Maass. Contour Reconstruction in 3-D X-Ray CT. *IEEE Transactions on Medical Imaging*, 12(4), December 1993.
- [24] A. Moreno, I. Bloch, J. Dutreuil, and M. Deval. 3D regularized reconstruction from a small number of projections in maxillo-facial imaging: feasibility and first experimental results. In *12ème Forum des Jeunes Chercheurs en GBM (Génie Biologique et Médical)*, pages 136–137, Nantes, France, May 2003.

- [25] K. Mueller, R. Yagel, and J.J. Wheller. Accurate low-contrast 3D cone-beam reconstruction with algebraic methods.
- [26] E. Payot, R. Guillemaud, Y. Troussel, and F. Prêteux. An adaptative and constrained model for 3D X-Ray vascular reconstruction. In *International Meeting on Fully Three-Dimensional Image Reconstruction in Radiology and Nuclear Medicine*, pages 19–23, Aix-les-Bains, Savoie, France, July 1995.
- [27] C. Pellet. *Reconstruction tridimensionnelle des bifurcations vasculaires à partir de deux projections en angiographie numérisée*. PhD thesis, Université Paris XI, October 1991.
- [28] F. Peyrin. *Méthodes de reconstruction d'images 3D à partir de projections coniques de rayons X*. PhD thesis, 90ISAL0028, Institut National des Sciences Appliquées (INSA) de Lyon and Université Claude Bernard (UCB) Lyon I, 1990.
- [29] F. Peyrin, L. Garnero, and I. Magnin. Reconstruction tomographique d'images 2D et 3D. *Traitement du signal*, 13(4):406–440, 1996.
- [30] S. Reboul, A. Taleb-Ahmed, M.M. Rousset, F. Wattrelot, and J.P. Dubus. Reconstruction d'objets binaires à partir de deux projections orthogonales par une technique inspirée de la théorie des graphes : la recherche du flût maximum à coût minimum. *Traitement du signal*, 12(15):327–341, 1995.
- [31] M. Ricard. *Imagerie par rayons X*. Cours du module SIM (Systèmes d'Imagerie Médicale), École Nationale Supérieure des Télécommunications, département TSI, 2000.
- [32] B. Robert. *Echographie tridimensionnelle*. PhD thesis, ENST 99E023, Ecole Nationale Supérieure des Télécommunications, Paris, October 1999.
- [33] A. Rougée, K.M. Hanson, and D. Saint-Félix. Comparison of 3-D tomographic algorithms for vascular reconstruction. In *SPIE 914*, pages 397–405, 1988.
- [34] E. Roullot. *Analyse d'acquisitions multiples anisotropes en angiographie par résonance magnétique 3D: modélisation et reconstruction régularisée pour l'amélioration de la résolution spatiale*. PhD thesis, ENST 2001E035, Ecole Nationale Supérieure des Télécommunications, Paris, December 2001.
- [35] L. A. Shepp and Y. Vardi. Maximum likelihood reconstruction for emission tomography. In *IEEE Transactions on Medical Imaging*, volume 1, pages 113–122, 1982.
- [36] P. Grangeat (sous la direction de). *La tomographie - Fondements mathématiques, imagerie microscopique et imagerie industrielle*. Hermès, Traité IC2, 2002.
- [37] J.P. Thirion. Segmentation of tomographic data without tomographic reconstruction. In *IEEE Transactions on Medical Imaging*, volume 11(1), pages 102–110, March 1992.
- [38] A. N. Tikhonov. Regularization of incorrectly posed problems. In *Soviet Math. Dokl.*, volume 4, pages 1624–1627, 1963.

- [39] Y. Troussset, D. Saint-Félix, A. Rougée, and C. Chardenon. Multiscale cone beam X-ray reconstruction. In *SPIE 1231*, pages 229–238, 1990.